



NUMERICAL FLOW SIMULATION  
ME-474

---

ASSIGNMENT 2

GROUND EFFECT ON AN AIRFOIL  
GROUP 27

MICHELE POLI - *michele.poli@epfl.ch* - 342543  
ALEXANDRO MAJOCCHI - *alexandro.majocchi@epfl.ch* - 346190  
SARAH NAILI - *sarah.naili@epfl.ch* - 363174  
MIGUEL MOOR - *miguel.moorcastro@epfl.ch* - 329379



AUTUMN SEMESTER 2025  
ÉCOLE POLYTECHNIQUE FÉDÉRALE DE LAUSANNE

## Table des matières

<b>1</b>	<b>Introduction</b>	<b>3</b>
1.1	Background and Literature Overview . . . . .	3
1.2	Objective of the Present Study . . . . .	3
1.3	Type of Analysis and Methodology . . . . .	4
<b>2</b>	<b>Geometrical Modeling</b>	<b>6</b>
2.1	Presentation of the airfoil geometry . . . . .	6
2.2	Presentation of the Domain Geometry . . . . .	6
2.3	Unit system . . . . .	8
2.4	Characteristic dimensions . . . . .	9
2.5	Symmetry and Periodicity of the Problem . . . . .	10
2.6	Geometrical space . . . . .	10
<b>3</b>	<b>Physical modeling and hypotheses</b>	<b>11</b>
3.1	Physical Behavior . . . . .	11
3.2	Fluid Properties . . . . .	11
3.3	Turbulent flow calculation . . . . .	11
<b>4</b>	<b>Boundary conditions, external forces, initial conditions</b>	<b>13</b>
4.1	Boundary conditions . . . . .	13
4.2	External forces . . . . .	14
4.3	Initial conditions . . . . .	14
<b>5</b>	<b>Computational mesh</b>	<b>15</b>
5.1	Mesh type . . . . .	15
5.2	Cell type . . . . .	16
5.3	Size and number of cells . . . . .	16
5.4	Boundary-layer treatment . . . . .	16
5.5	Mesh quality and final mesh . . . . .	17
<b>6</b>	<b>Numerical methods</b>	<b>19</b>
6.1	Spatial discretization method . . . . .	19
6.2	Type of simulation and solver . . . . .	19
6.3	Solution options and convergence criteria . . . . .	20
6.4	Computed quantities . . . . .	20
<b>7</b>	<b>Mesh size / domain size convergence study</b>	<b>22</b>
7.1	Objective and convergence criterion . . . . .	22
7.2	Reference configurations and methodology . . . . .	22
7.3	Mesh parameters . . . . .	22
7.4	Domain size convergence study . . . . .	23
7.5	Mesh size convergence study . . . . .	24
7.6	Error estimation . . . . .	31
7.7	Choice of the mesh and the domain . . . . .	33

<b>8</b>	<b>Results</b>	<b>34</b>
8.1	Pressure and Velocity Contours . . . . .	34
8.2	Aerodynamic Coefficients in Ground Effect . . . . .	37
<b>9</b>	<b>Analysis and Conclusions</b>	<b>39</b>
9.1	Summary of Results . . . . .	39
9.2	Drag Behavior at Low Ground Clearance . . . . .	39
9.3	Comparison with Experimental Literature . . . . .	40
9.4	Accuracy and Limitations . . . . .	40
9.5	Implications for Real Ground-Effect Vehicles . . . . .	41
9.6	Conclusions . . . . .	41
9.7	Recommendations . . . . .	42
<b>10</b>	<b>Appendix</b>	<b>43</b>

# 1 Introduction

This chapter introduces the physical background and the objectives of the present study. First, a brief overview of the existing literature on ground-effect aerodynamics is provided. The specific configuration investigated in this work is then presented, followed by a description of the type of analysis and the general numerical methodology adopted.

## 1.1 Background and Literature Overview

The aerodynamic performance of lifting surfaces can change significantly when an aircraft operates in close proximity to the ground. This phenomenon, commonly referred to as the *ground effect*, alters the pressure distribution around the wing and generally leads to an increase in lift together with a reduction of induced drag. Due to its importance during takeoff, landing, and sustained low-altitude flight, ground effect has been extensively investigated using analytical, experimental, and numerical approaches.

Early studies by Maskell [3] and Liu and Patel [4] employed potential-flow models to analyze how the modification of downwash and the confinement of the flow near the ground affect lift and pitching moment. More advanced numerical investigations, such as the Reynolds-Averaged Navier-Stokes (RANS) simulations performed by Hsiun and Chen [5], showed that airfoil aerodynamic performance becomes highly sensitive to ground clearance, particularly when the wing operates at very small ride heights.

Subsequent works shifted the focus toward parametric studies on airfoils operating in ground effect. Ahmed and Sharma [6], as well as Qu et al. [8], demonstrated that the aerodynamic benefits associated with ground effect strongly depend on both the angle of attack and the ratio between ground clearance and chord length. Research on Wing-in-Ground (WIG) vehicles, such as the work done by Rozhdestvensky [9], further emphasized how low-altitude aerodynamic effects can be exploited to improve efficiency during sustained near-ground operations. In addition, studies addressing more complex wing configurations or control devices—for instance those by Ockfen and Matveev [10]—indicated that planform geometry and flap deployment can significantly amplify or mitigate ground-effect phenomena.

Despite the wide range of configurations examined, the literature consistently reports that :

- lift increases as the ground clearance decreases,
- induced drag is reduced,
- the pitching moment may shift, often in a nose-up direction,
- the influence of ground effect becomes negligible once the clearance exceeds a characteristic wing length scale, typically the chord.

Most studies consider an idealized flat and rigid ground surface, which provides a consistent and reliable reference for comparing the aerodynamic behavior of different wing geometries.

## 1.2 Objective of the Present Study

The present work investigates the aerodynamic effects associated with the proximity of a lifting surface to the ground, taking inspiration from the wing of the Alexeyev KM Ekranoplan, also known as the *Caspian Sea Monster*. The KM represents a historically significant example of a WIG vehicle, specifically designed to operate efficiently within the ground-effect regime.

The objective of this study is not to reproduce the exact geometry of the KM wing (since the real data are classified), but rather to analyze the fundamental aerodynamic trends related to the ground effect using a simplified and idealized configuration. A two-dimensional airfoil representative of a typical lifting surface is therefore considered, allowing the influence of ground clearance on the aerodynamic behavior to be isolated and studied in a controlled manner.

In particular, the aim of the present work is to quantify how the lift and drag coefficients vary as a function of ground clearance. Several ride heights are investigated, including a reference case corresponding to effectively infinite clearance. By comparing these configurations, the study seeks to characterize the onset, magnitude, and decay of ground-effect phenomena, and to provide qualitative and quantitative insight into the aerodynamic performance of lifting surfaces operating close to the ground.



FIGURE 1 – Alexeyev KM Ekranoplan

### 1.3 Type of Analysis and Methodology

The present study is based on a series of two-dimensional Computational Fluid Dynamics (CFD) simulations performed using ANSYS Fluent, with the aim of quantifying the influence of ground proximity on the aerodynamic performance of a representative wing section. A two-dimensional approach is adopted in order to focus on the fundamental aerodynamic mechanisms associated with ground effect, while neglecting three-dimensional effects such as wing-tip vortices.

All simulations are carried out under controlled conditions, in which the freestream properties and operating parameters are kept constant. In particular, air density is set to standard atmospheric conditions, the freestream velocity is chosen to be representative of low-altitude flight, and the angle of attack is kept identical for all simulated cases. As a result, any variation observed in the aerodynamic coefficients can be directly attributed to changes in ground clearance.

Although the freestream Mach number is close to the lower limit of the compressible regime ( $\text{Ma} \approx 0.36$ ), the flow is modeled as incompressible. This assumption is considered appropriate for the present comparative study, as compressibility effects are expected to be secondary and to affect all ground-clearance configurations in a similar manner.

The numerical model consists of a two-dimensional computational domain containing a NACA 4412 airfoil, selected as a representative lifting-surface geometry. Several simulations are performed for different ground clearance ratios, including a reference configuration corresponding to effectively infinite clearance, which serves as a baseline for comparison.

Turbulence effects are modeled using a RANS approach. In particular, the Spalart–Allmaras one-equation turbulence model is employed in order to accurately capture boundary-layer behavior in the vicinity of the airfoil.

The detailed description of the airfoil geometry, computational domain, boundary conditions, mesh generation strategy, and numerical solution procedures is provided in the following sections. The aerodynamic coefficients obtained from the simulations are finally analyzed and compared in order to assess the impact of ground proximity on lift and drag, in relation to theoretical expectations and trends reported in the literature.

## 2 Geometrical Modeling

This chapter describes the geometrical configuration adopted for the numerical simulations. The airfoil geometry, the dimensionality assumptions, the computational domain, and the main characteristic dimensions are presented.

### 2.1 Presentation of the airfoil geometry

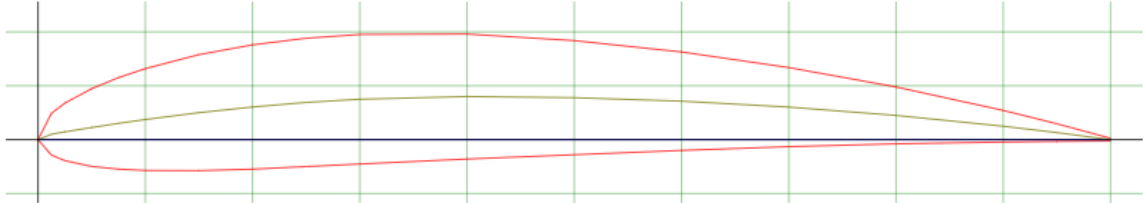


FIGURE 2 – Two-dimensional geometry of the NACA 4412 airfoil imported from AirfoilTools.

The lifting surface considered in this study is based on a NACA 4412 airfoil. This airfoil was chosen as a representative cambered profile commonly used in aircraft applications and exhibiting well-documented aerodynamic behavior.

The airfoil geometry was generated using the AirfoilTools database [11], which provides a set of normalized coordinates describing the airfoil profile. The coordinate data were downloaded in spreadsheet format and subsequently converted to a plain text file (`.txt`). These coordinates were uniformly scaled to obtain a chord length of [2]

$$c = 18.8 \text{ m.}$$

The resulting text file was imported into ANSYS DesignModeler via *Concept → 3D Curve*, which reads the point coordinates and generates a spline curve defining the airfoil boundary.

The airfoil chord is aligned with the global  $x$ -axis of the computational domain, and the angle of attack is fixed at  $\alpha = 0^\circ$  for all simulations.

### 2.2 Presentation of the Domain Geometry

The computational domain is designed to represent an external aerodynamic flow around the airfoil while minimizing artificial confinement effects. Two domain configurations are employed in this study, differing in both the treatment of the lower boundary and the upstream geometry.

#### Reference Configuration (Infinite Ground Clearance)

In the reference case, the domain is composed of a semi-circular inlet region upstream and a rectangular region downstream, as illustrated in Fig. 3. The use of a semi-circular inlet is a common practice in external aerodynamic simulations, ensuring that the inflow boundary is located at a constant distance from the airfoil in all upstream directions. This helps preserve a uniform and undisturbed freestream condition, reduces spurious numerical effects associated with corner singularities, and aligns naturally with the expected streamlines approaching an isolated airfoil.

The inlet boundary is located at a distance of  $5c$  upstream of the airfoil leading edge. The outlet boundary is positioned  $10c$  downstream of the trailing edge, and the upper and lower boundaries are located  $5c$  from the airfoil. These distances ensure that the incoming flow remains weakly influenced by the airfoil presence and that the wake develops without numerical interference from domain boundaries.

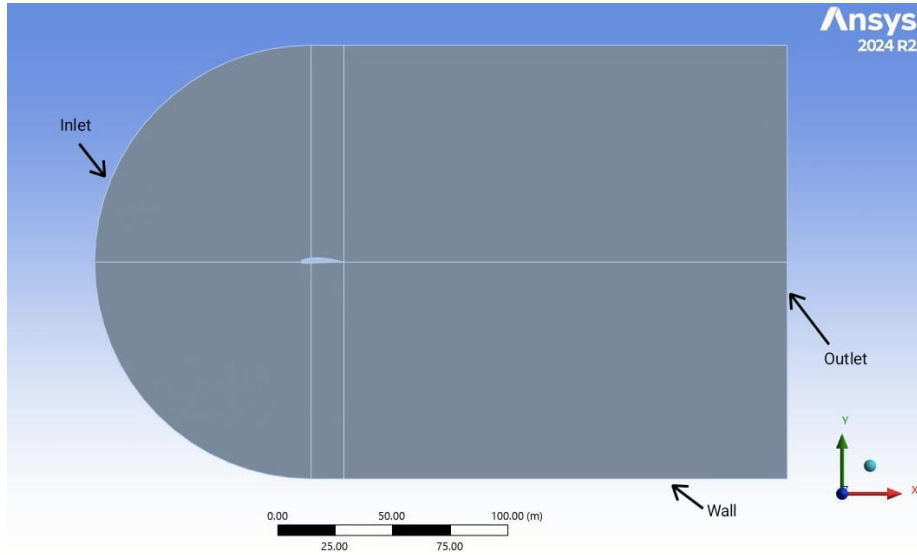


FIGURE 3 – Computational domain for the reference case (infinite ground clearance).

### Ground-Effect Configuration

For ground-effect cases, the domain geometry is modified to accommodate the presence of a solid ground surface. The upstream region consists of a quarter-circle arc connected to a vertical straight segment extending down to the ground level, as shown in Fig. 4. This configuration maintains a smooth inflow boundary while ensuring compatibility with the flat ground surface.

The ground clearance is characterized by the non-dimensional height-to-chord ratio  $h/c$ , where  $h$  is the vertical distance from the lowest point of the airfoil to the ground. The values investigated in this study are :

$$h/c = 2.0, 1.0, 0.5, 0.25.$$

The upper boundary remains at  $5c$  above the airfoil, and the outlet is positioned  $10c$  downstream of the trailing edge, consistent with the reference configuration.

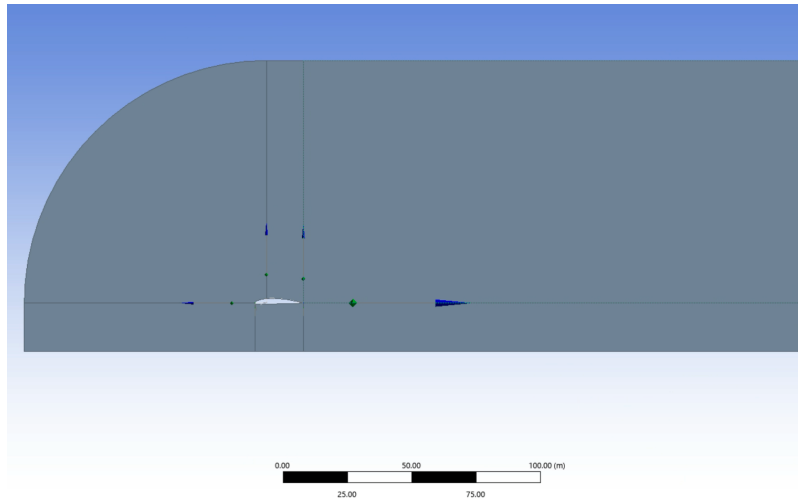


FIGURE 4 – Computational domain for ground-effect cases (shown here for  $h/c = 1.0$ ).

From an operational perspective, WIG vehicles are typically designed to operate at small height-to-chord ratios where ground-effect benefits are maximized. An optimal operating height of approximately  $h/c = 0.25$  is often reported for ekranoplans, corresponding to maximum aerodynamic efficiency.

For all configurations, the freestream velocity is kept constant at  $V = 125$  m/s, allowing the influence of ground proximity on the aerodynamic coefficients to be isolated without introducing Reynolds number variations.

### 2.3 Unit system

All physical quantities in the simulations are expressed using the International System of Units (SI). The main units employed in this study are summarized in Table 1.

Physical quantity	SI unit
Length	m
Mass	kg
Time	s
Velocity	$\text{m s}^{-1}$
Density	$\text{kg m}^{-3}$
Pressure	Pa
Dynamic viscosity	$\text{Pas}$
Force	N

TABLE 1 – Main physical quantities and corresponding SI units used in this study

## 2.4 Characteristic dimensions

The characteristic length scale of the problem is the airfoil chord length,  $L = c = 18.8$  m. The freestream velocity is set to  $V = 125$  m/s. Based on these values, the Reynolds number is defined as

$$\text{Re} = \frac{\rho V L}{\mu} = \frac{V L}{\nu}, \quad (1)$$

where  $\nu = 1.46 \times 10^{-5}$  m<sup>2</sup>/s is the kinematic viscosity of air under standard atmospheric conditions. This yields

$$\text{Re} = \frac{125 \times 18.8}{1.46 \times 10^{-5}} \approx 1.6 \times 10^8,$$

indicating a fully turbulent flow regime, since  $\text{Re} \gg 10^4$ . As a consequence, thin boundary layers are expected to develop both on the airfoil surface and on the ground.

An estimate of the boundary-layer thickness on the airfoil is required to assess near-wall resolution requirements and to justify the turbulence modeling strategy. Given the high Reynolds number of the flow ( $\text{Re} \approx 1.6 \times 10^8$ ), the boundary layer is assumed to be fully turbulent over most of the airfoil surface.

A first-order estimate of the turbulent boundary-layer thickness can be obtained using the classical flat-plate correlation for turbulent flow :

$$\delta(x) \approx 0.37 x \text{Re}_x^{-1/5}, \quad (2)$$

where  $\text{Re}_x = Ux/\nu$  is the Reynolds number based on the streamwise distance  $x$  from the leading edge.

Taking a characteristic length  $x \approx c = 18.8$  m yields

$$\delta_{\text{airfoil}} \approx 0.37 \times 18.8 \times (1.6 \times 10^8)^{-1/5} \approx 0.1 \text{ m}. \quad (3)$$

This estimate indicates that the boundary layer remains thin compared to the airfoil chord ( $\delta/c \sim 5 \times 10^{-3}$ ), but thicker than a laminar boundary layer at the same Reynolds number. This justifies the use of a turbulence model and a dedicated near-wall mesh treatment.

The ground boundary layer is strongly reduced but not strictly absent, since the ground is modeled as a moving wall with tangential velocity equal to the freestream velocity. This choice ensures negligible relative shear between the fluid and the ground in the airfoil reference frame. The near-wall treatment and mesh resolution strategy are described in detail in Section 5.

To determine whether fluid compressibility effects should be considered, we calculate the Mach number, defined as :

$$\text{Ma} = \frac{V}{a} \quad (4)$$

where  $V$  is the flow velocity and  $a$  is the speed of sound in air.

For air at  $T = 25^\circ\text{C}$  and  $p = 1$  atm, the speed of sound is approximated as :

$$a = \sqrt{\gamma R T} \quad (5)$$

with  $\gamma = 1.4$ ,  $R = 287$  J/(kg · K), and  $T = 298$  K. Substituting the values yields  $a \approx 347$  m/s. Thus, the Mach number at  $V = 125$  m/s is  $\text{Ma} \approx 0.36$ .

This value lies at the upper limit of the incompressible regime. The density variation due to compressibility can be estimated using the isentropic relation [12] :

$$\frac{\rho}{\rho_0} = \left( 1 + \frac{\gamma - 1}{2} Ma^2 \right)^{-\frac{1}{\gamma-1}} \quad (6)$$

For air with  $\gamma = 1.4$  and  $Ma = 0.36$  :

$$\frac{\rho}{\rho_0} = \left( 1 + \frac{0.4}{2} \times 0.36^2 \right)^{-2.5} = (1.026)^{-2.5} \approx 0.937 \quad (7)$$

This corresponds to a density error of approximately 6–7% when neglecting compressibility effects. However, this modeling choice is consistent with the incompressible RANS framework, which is commonly considered valid for external aerodynamic flows up to  $Ma < 0.4$ . Since the resulting density error affects all simulated configurations in the same manner, it does not compromise the validity of relative comparisons between different ground-clearance cases.

## 2.5 Symmetry and Periodicity of the Problem

The present problem does not exploit geometrical symmetry or periodicity. Although the airfoil geometry is symmetric with respect to the mid-span plane, the presence of the ground breaks the vertical symmetry of the flow configuration.

In addition, no periodic boundary conditions are applicable. The boundary conditions, external forces, and expected flow features are therefore not periodic in any direction.

As a consequence, the full two-dimensional domain described in the previous sections is retained for all simulations.

## 2.6 Geometrical space

The flow is modeled as two-dimensional. This assumption is justified by the following considerations :

- the flow is assumed to be far from the wing tips, such that three-dimensional end effects are negligible,
- the airfoil geometry does not vary along the spanwise ( $z$ ) direction,
- the velocity component in the  $z$  direction is neglected.

Under these assumptions, the flow can be treated as planar, allowing the main aerodynamic mechanisms associated with ground effect to be investigated while keeping the computational cost reasonable.

### 3 Physical modeling and hypotheses

#### 3.1 Physical Behavior

The fluid considered in this study is air, which is modeled as a Newtonian fluid. Under the operating conditions investigated, the relationship between shear stress and strain rate is assumed to be linear, with a constant dynamic viscosity.

As justified in Section 2.4, the flow is modeled as incompressible despite a Mach number of  $\text{Ma} \approx 0.36$ . The flow is therefore treated with constant density and viscosity.

Thermal effects are not explicitly modeled. Heat transfer between the fluid and the airfoil, as well as viscous heating, are neglected. No energy equation is solved, and the flow is treated as aerodynamically driven.

Furthermore, the flow is considered to be single-phase, and no multiphase effects are taken into account. Chemical reactions, combustion phenomena, and species transport are not included in the present simulations.

These modeling assumptions allow the aerodynamic behavior associated with ground effect to be investigated while keeping the physical model consistent with the objectives of the study.

#### 3.2 Fluid Properties

The fluid considered in the present study is air, and its physical properties are defined assuming standard atmospheric conditions. The reference temperature and pressure are set to  $T = 25^\circ\text{C}$  and  $p = 1 \text{ bar}$ , respectively.

Under these conditions, the air density is assumed to be constant and equal to

$$\rho = 1.225 \text{ kg/m}^3.$$

The kinematic viscosity of air is taken as

$$\nu = 1.46 \times 10^{-5} \text{ m}^2/\text{s},$$

which corresponds to a dynamic viscosity of

$$\mu = 1.7894 \times 10^{-5} \text{ Pa} \cdot \text{s}.$$

These properties are used consistently in all simulations and are representative of air under standard atmospheric conditions.

#### 3.3 Turbulent flow calculation

Given the high Reynolds number of the flow ( $\text{Re} \approx 1.6 \times 10^8$ ), the flow is fully turbulent. Turbulence effects are therefore modeled using a RANS approach.

The Spalart–Allmaras one-equation turbulence model is employed in this study. This model is specifically designed for external aerodynamic flows and has been widely validated for airfoil applications. It provides an efficient and accurate description of boundary-layer-dominated flows at a reduced computational cost compared to two-equation models.

The near-wall treatment is implicitly determined by the mesh resolution, resulting in a wall-function-type behavior consistent with the achieved  $y^+$  values. Accordingly, the computational mesh

is designed to adequately resolve the near-wall region, with  $y^+$  values ranging approximately from 8 to 200 along the airfoil surface. Details on the resulting  $y^+$  values are provided in Section 5.4. The same near-wall meshing strategy is applied to all simulated configurations to ensure consistency when comparing different ground-clearance cases.

## 4 Boundary conditions, external forces, initial conditions

The simulations are performed in the reference frame of the airfoil. The airfoil is therefore modeled as a stationary body, while the airflow enters the computational domain through a velocity inlet and exits through a pressure outlet. The aircraft is assumed to move at constant velocity in straight flight, and no non-inertial or fluid–structure interaction effects are considered.

### 4.1 Boundary conditions

The boundary conditions applied to the computational domain are defined to reproduce an external aerodynamic flow in the presence of a ground surface. They are summarized below and illustrated in Fig. 5.

- **Velocity inlet** : Velocity inlet : a uniform freestream velocity of  $V = 125$  m/s is imposed at the inlet boundary. The velocity vector is aligned with the airfoil chord. A low turbulent viscosity ratio ( $\mu_t/\mu = 1$ ) is prescribed at the inlet, corresponding to a weakly turbulent freestream typical of external aerodynamic flows. This choice is consistent with the use of the Spalart–Allmaras turbulence model, in which turbulence is primarily generated by local shear within the boundary layers developing on the airfoil and on the ground. The same inlet turbulence conditions are applied to all simulated configurations to ensure a consistent comparison between different ground-clearance cases.
- **Pressure outlet** : the outlet boundary is defined as a pressure outlet with a gauge pressure of 0 Pa (atmospheric pressure). This choice ensures a well-posed outlet condition for external aerodynamic flow simulations by allowing the velocity field to develop naturally while enforcing the correct static pressure level.
- **Airfoil surface** : the airfoil is modeled as a no-slip stationary wall. Both pressure and viscous shear stresses are computed on the surface in order to evaluate the aerodynamic forces.
- **Ground** : the lower boundary of the domain is modeled as a no-slip wall. To correctly represent the relative motion between the airfoil and the ground in the airfoil reference frame, the ground is treated as a moving wall with a tangential velocity equal to the freestream velocity. This choice ensures zero relative velocity between the fluid and the ground, thereby preventing the development of spurious shear stresses and non-physical boundary-layer effects associated with a stationary ground in this reference frame.
- **Upper boundary (and also lower boundary in the case without ground)** : the upper boundary of the domain is treated as a zero shear stress wall, preventing normal velocity penetration while minimizing shear effects and artificial confinement of the flow.

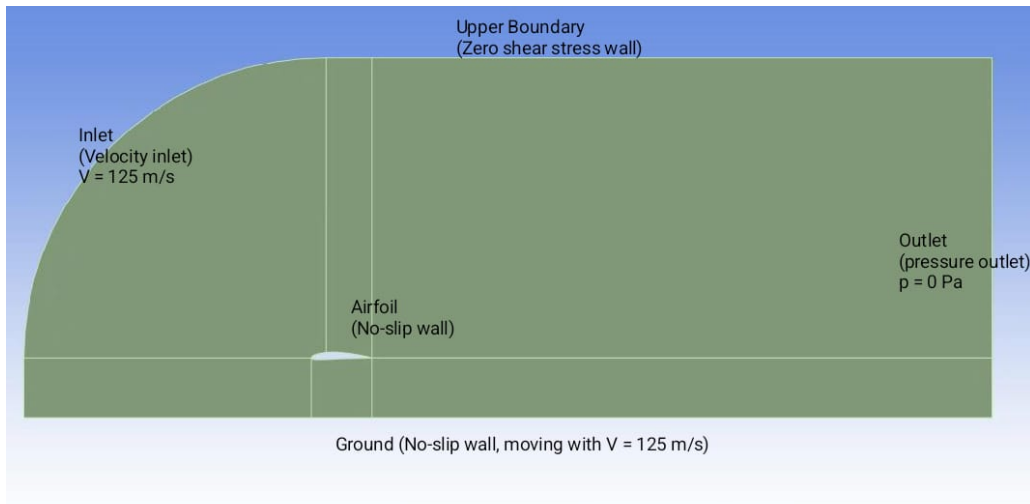


FIGURE 5 – Overview of the computational domain and applied boundary conditions.

## 4.2 External forces

No external body forces are explicitly imposed in the numerical model. Gravity is neglected, as it does not directly influence the aerodynamic forces acting on the airfoil in steady horizontal flight.

The only forces computed in the simulations are the aerodynamic forces resulting from pressure and viscous shear stress distributions on the airfoil surface. These forces are used to evaluate the lift and drag coefficients.

## 4.3 Initial conditions

All simulations are performed under steady-state conditions. As a result, no physical initial conditions are required.

From a numerical standpoint, the flow field is initialized using the standard initialization procedure available in ANSYS Fluent. The choice of initial conditions only affects the convergence behavior of the solver and does not influence the final converged solution.

## 5 Computational mesh



FIGURE 6 – Final computational mesh used for the ground-effect simulations, shown for the  $h/c = 0.25$  configuration.

Figure 6 shows the computational mesh for the  $h/c = 0.25$  configuration, which represents the most constrained ground-clearance case investigated in this study. This configuration is selected for illustration because it requires the highest mesh density in the gap region between the airfoil and the ground, and therefore represents the most demanding case in terms of mesh quality. For larger ground clearances ( $h/c = 0.5, 1.0, 2.0$ , and  $\infty$ ), the same meshing strategy is applied, with the only difference being the vertical position of the ground boundary (or its absence in the  $h/c = \infty$  case). The mesh topology, edge sizing parameters, and refinement zones remain consistent across all configurations to ensure meaningful comparisons of aerodynamic coefficients.

The accuracy of CFD simulations strongly depends on the quality of the computational mesh, especially in the presence of thin boundary layers and confined flow regions such as those encountered in ground-effect configurations. In the present study, particular attention was paid to mesh structure, near-wall resolution, and overall mesh quality to ensure reliable prediction of aerodynamic forces.

### 5.1 Mesh type

A structured mesh was adopted for all simulations. The computational domain was discretized using a mapped meshing strategy, resulting in an ordered grid that is predominantly aligned with the freestream direction in the far-field regions, while allowing local adaptation to the airfoil geometry and near-wall flow.

The choice of a structured mesh is motivated by the following considerations :

- improved numerical accuracy for external aerodynamic flows,
- better control of cell distribution and stretching,
- reduced numerical diffusion compared to unstructured meshes,
- easier refinement of regions of interest such as the boundary layer, wake, and the gap between the airfoil and the ground.

In particular, the structured layout allows the mesh to follow the airfoil geometry smoothly and to align the cells with the expected flow direction, which is essential for accurate resolution of pressure and velocity gradients.

## 5.2 Cell type

The mesh is composed exclusively of quadrilateral cells. No triangular elements are used.

Quadrilateral elements were chosen because :

- they provide higher accuracy for resolving boundary-layer flows,
- exhibit lower numerical dissipation when aligned with the flow,
- allow higher aspect ratios near walls while maintaining acceptable mesh quality.

This choice is particularly suitable for RANS simulations of external aerodynamic flows.

## 5.3 Size and number of cells

The mesh resolution is non-uniform and adapted to the physical features of the flow. Local refinements are applied in regions where large gradients are expected, while coarser cells are used in the far-field regions to reduce computational cost.

The main refinement zones are :

- **Around the airfoil** : fine mesh to accurately capture pressure gradients and boundary-layer development.
- **Between the airfoil and the ground** : increased resolution to resolve the confined flow responsible for the ground-effect phenomenon.
- **Wake region** : moderate refinement downstream of the trailing edge to capture velocity deficit and shear layers.

Cell sizing is controlled using edge sizing with bias factors, allowing a gradual transition from fine cells near the airfoil surface to larger cells in the far field. This avoids abrupt changes in cell size and helps maintain good mesh quality.

The total number of cells depends on the considered ground clearance and on the mesh refinement level used for convergence studies. For the final simulations, the number of cells ranges from approximately 8,000 (coarsest mesh) to 140,000 (finest mesh), corresponding to cell counts between  $\mathcal{O}(10^4)$  and  $\mathcal{O}(10^5)$  depending on the configuration and mesh refinement level.

## 5.4 Boundary-layer treatment

A dedicated near-wall mesh refinement is applied around the airfoil surface in order to correctly resolve the boundary layer. The smallest cells are located directly at the airfoil wall, with a progressive growth in the wall-normal direction.

The turbulence modeling approach relies on wall functions, and the near-wall mesh is designed to achieve wall-normal resolution compatible with this assumption. The dimensionless wall distance  $y^+$  is monitored a posteriori in Fluent to ensure that the obtained values are consistent across all simulated configurations.

The first cell height near the airfoil surface was sized to achieve  $y^+$  values in the range of 8–204, which falls within acceptable limits for the Spalart–Allmaras turbulence model with wall functions. The minimum values ( $y^+ \approx 8$ ) occur near the leading edge where the boundary layer is thin, while the maximum values ( $y^+ \approx 204$ ) are found near the trailing edge due to boundary-layer growth.

Although the exact  $y^+$  values vary along the airfoil surface, the same meshing strategy is applied to all ground-clearance cases. This ensures that relative comparisons of aerodynamic coefficients between different values of  $h/c$  remain meaningful and consistent.

It is important to note that no boundary-layer refinement is applied near the ground surface. Since the ground is modeled as a moving wall with a tangential velocity equal to the freestream velocity (see Section 4.1), there is no relative motion between the fluid and the ground, and consequently no boundary layer develops on the ground. This modeling choice is physically consistent with the airfoil reference frame adopted in this study, where the airfoil is stationary and the ground moves beneath it at the flight speed.

## 5.5 Mesh quality and final mesh

The quality of the final mesh is assessed using standard mesh quality metrics provided by Fluent, including :

- orthogonal quality,
- skewness,
- aspect ratio.

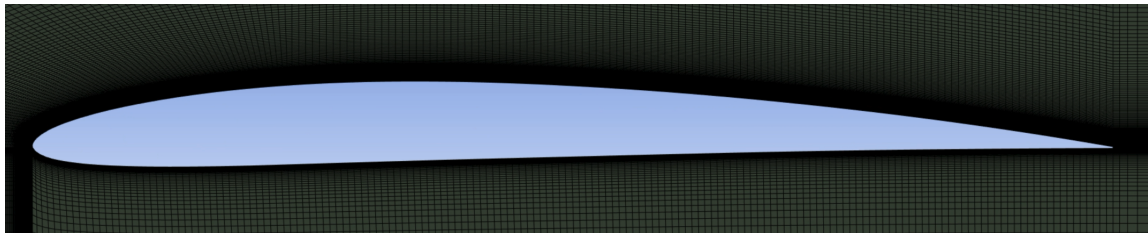
Table 2 summarizes the mesh quality metrics obtained for a representative configuration.

Metric	Value	Criterion
Orthogonal Quality (min)	0.10	> 0.1
Skewness (max)	0.74	< 0.9
Aspect Ratio (max)	$\sim 10^5$	Acceptable in BL

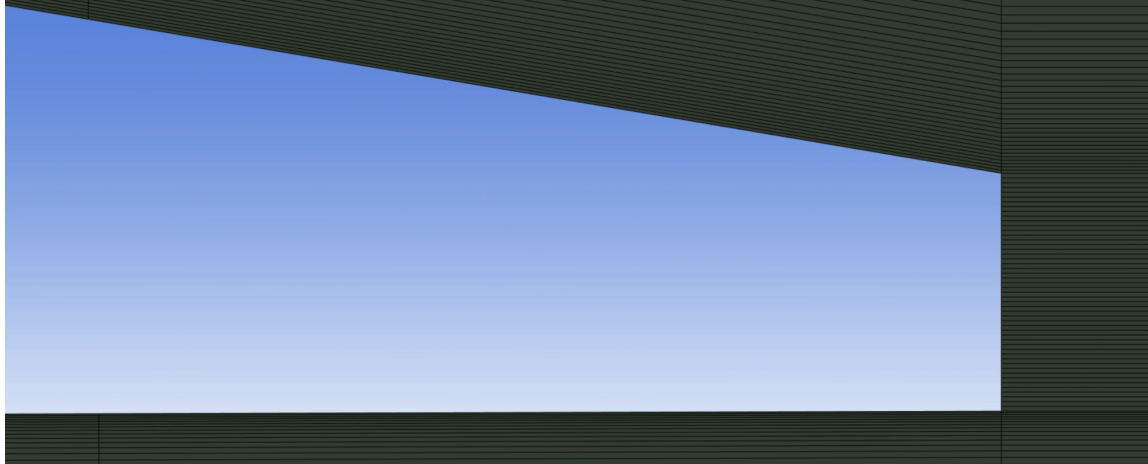
TABLE 2 – Mesh quality metrics for a representative ground-effect configuration.

The minimum orthogonal quality and maximum skewness values remain within acceptable limits for RANS simulations. High aspect-ratio cells are mainly located in near-wall regions, where elongated cells aligned with the flow are desirable for boundary-layer resolution.

A close-up view of the mesh around the airfoil is shown in Fig. 7.



(a) Overview around the airfoil



(b) Detail of the trailing edge

FIGURE 7 – Structured mesh around the NACA 4412 airfoil for the  $h/c = 0.25$  configuration : (a) overview showing the refinement zone around the airfoil, and (b) close-up of the trailing edge showing the near-wall cell distribution.

## 6 Numerical methods

The numerical simulations are performed using the finite volume solver ANSYS Fluent. This section describes the discretization approach, the type of solver and simulation, the solution algorithms, and the computed quantities of interest.

### 6.1 Spatial discretization method

Fluent relies on the finite volume method (FVM) to discretize the governing equations. The computational domain is divided into a finite number of control volumes, and the integral form of the conservation equations is solved over each cell.

Pressure interpolation is performed using the second-order scheme available in ANSYS Fluent, while second-order upwind discretization is employed for the momentum and turbulence equations.

The use of second-order schemes reduces numerical diffusion and improves the accuracy of the predicted pressure and velocity fields, which is particularly important for the correct evaluation of aerodynamic forces such as lift and drag.

### 6.2 Type of simulation and solver

The numerical simulations are performed using ANSYS Fluent and are based on a steady-state, two-dimensional RANS formulation. Since the flow Mach number is  $\text{Ma} \approx 0.36$ , the flow is modeled as incompressible with constant density and viscosity, as justified in Section 2.4. A pressure-based segregated solver is therefore employed, which is well suited for steady incompressible flows and is commonly used for external aerodynamic simulations in the subsonic regime.

The governing equations solved in the present study are the incompressible RANS equations, consisting of the continuity equation

$$\nabla \cdot \mathbf{u} = 0, \quad (8)$$

and the momentum equations

$$\rho(\mathbf{u} \cdot \nabla)\mathbf{u} = -\nabla p + \nabla \cdot [(\mu + \mu_t)(\nabla \mathbf{u} + \nabla \mathbf{u}^T)], \quad (9)$$

where  $\mathbf{u}$  is the mean velocity vector,  $p$  is the mean pressure,  $\mu$  is the molecular dynamic viscosity, and  $\mu_t$  is the turbulent eddy viscosity obtained from the turbulence model.

Turbulence effects are modeled using the Spalart–Allmaras one-equation model, which solves an additional transport equation for a modified turbulent viscosity variable. The turbulent viscosity  $\mu_t$  is then computed from this variable and contributes to the closure of the RANS momentum equations. This model is specifically designed for external aerodynamic flows and provides a good compromise between accuracy and computational efficiency for boundary-layer-dominated configurations.

The simulations are performed under steady-state conditions. Pressure–velocity coupling is handled using the SIMPLE (Semi-Implicit Method for Pressure-Linked Equations) algorithm. Second-order spatial discretization schemes are employed for the momentum equations, pressure, and turbulence model to reduce numerical diffusion and improve the accuracy of the predicted aerodynamic forces.

Double-precision arithmetic in ANSYS Fluent is used to reduce round-off errors, particularly in the computation of aerodynamic forces. The pressure-based solver is used in segregated mode, and default under-relaxation factors are employed for all variables. These settings were found to provide stable convergence behavior for all investigated ground-clearance configurations.

### 6.3 Solution options and convergence criteria

The flow field is initialized using the standard initialization procedure available in ANSYS Fluent. No specific initial condition is required, since the simulations are steady-state. Convergence of the numerical solution is assessed using both algebraic and physical criteria :

- the scaled residuals of all governing equations (continuity, momentum, and turbulence equation) are required to drop below  $10^{-4}$ ;
- the aerodynamic force coefficients, namely the lift coefficient  $C_L$  and the drag coefficient  $C_D$ , are monitored during the iterations and must reach a stable plateau;
- mass conservation is verified by ensuring that the difference between the inlet and outlet mass flow rates is negligible.

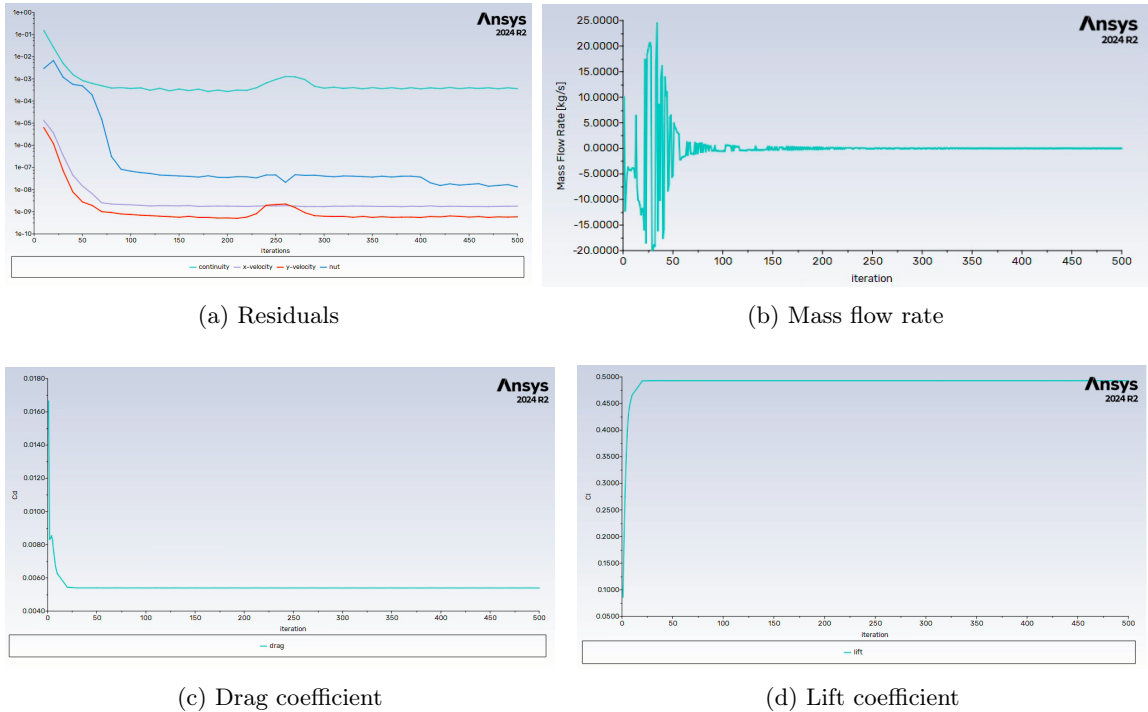


FIGURE 8 – Residuals, mass flow rate and aerodynamic coefficients for the case with  $h/c = 1$

All simulations are run for a maximum of 500 iterations. In practice, convergence is typically achieved well before reaching this limit. The combination of residual reduction, mass flow balance, and stabilization of integrated aerodynamic forces ensures that the solution is both numerically and physically converged.

### 6.4 Computed quantities

The primary quantities of interest computed in this study are the aerodynamic force coefficients acting on the airfoil :

- lift coefficient  $C_L$ ,
- drag coefficient  $C_D$ ,
- aerodynamic efficiency ratio  $C_L/C_D$ .

These coefficients are obtained by integrating the pressure and viscous shear stress distributions over the airfoil surface.

In addition to force coefficients, several flow-field quantities are extracted for qualitative analysis and validation of the physical behavior :

- pressure contours,
- velocity magnitude contours,
- streamlines,
- wall  $y^+$  distributions.

These fields are used to analyze the modification of the flow structure induced by ground proximity and to verify the consistency of the near-wall resolution and turbulence modeling.

## 7 Mesh size / domain size convergence study

A convergence study is performed in order to ensure that the numerical results are independent of both the computational domain size and the spatial discretization. Beyond verifying numerical convergence, the objective of this study is to identify the coarsest mesh that provides sufficiently accurate and stable aerodynamic coefficients, while keeping the computational cost reasonable.

The convergence analysis focuses on the lift coefficient  $C_L$  and the drag coefficient  $C_D$ , which are the primary quantities of interest in the present work.

### 7.1 Objective and convergence criterion

A solution is considered numerically converged when further refinement of the mesh or enlargement of the computational domain leads to variations smaller than 2% in both  $C_L$  and  $C_D$ .

This threshold is chosen as a compromise between numerical accuracy and computational efficiency and is commonly used in external aerodynamic CFD studies. The final objective of the convergence study is therefore to select the coarsest mesh that satisfies this convergence criterion.

### 7.2 Reference configurations and methodology

The  $h/c = 1$  configuration was selected for the convergence study because it represents an intermediate ground-effect case that captures the relevant physics without introducing excessive mesh constraints. Once mesh independence was verified for these two cases, the same meshing parameters (edge sizing, bias factors, and refinement zones) were applied to the remaining ground-clearance configurations ( $h/c = 2, 0.5$ , and  $0.25$ ), adjusting only the domain height accordingly. This approach ensures consistency across all simulations while avoiding redundant convergence studies for each configuration.

Mesh refinement follows a systematic approach, where the total number of cells is increased by a factor of approximately  $\sqrt{2}$  between successive meshes. This refinement strategy enables a consistent comparison between mesh levels and facilitates the estimation of discretization using Richardson extrapolation.

The number of mesh levels tested for each configuration is as follows :

- No ground (infinite clearance) : 5 meshes
- $h/c = 1$  : 6 meshes
- $h/c = 2, h/c = 0.5, h/c = 0.25$  : 1 mesh each (final mesh only, using parameters validated on  $h/c = 1$ )

For each configuration, the finest mesh that can be computed within a reasonable computational time is used as a reference solution for error estimation.

### 7.3 Mesh parameters

The mesh is controlled using edge sizing with specified number of divisions and bias factors to ensure proper refinement in critical regions. Table 3 summarizes the edge sizing parameters used for the  $h/c = 0.25$  configuration, which represents the most constrained case. The correspondence between each edge sizing number and its location in the computational domain is illustrated in Fig. 9.

Edge Sizing	Number of Divisions	Bias Factor
1	30	300
2	165	No bias
3	120	No bias
4	70	No bias
5	250	5000
6	65	1500
7	50	No bias

TABLE 3 – Edge sizing parameters for the  $h/c = 0.25$  configuration.

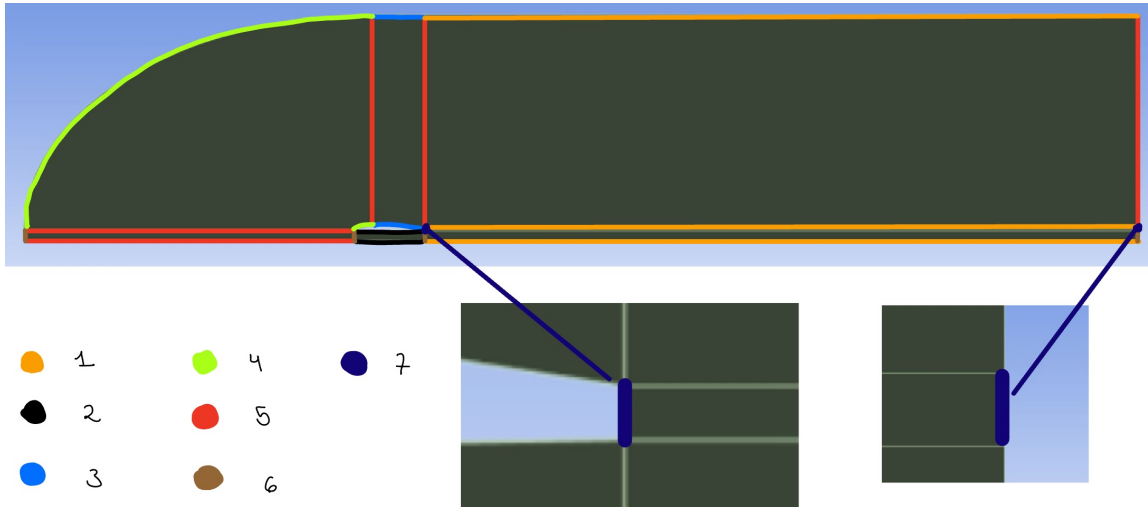


FIGURE 9 – Location of each edge sizing in the computational domain.

Similar meshing parameters are applied to the other ground-clearance configurations proportionally to the  $h/c$  factor.

#### 7.4 Domain size convergence study

Before investigating mesh convergence, the influence of the computational domain size is assessed. The upstream, downstream, and upper boundaries of the domain are progressively moved farther away from the airfoil, while keeping the mesh resolution near the airfoil unchanged.

The convergence with respect to domain size is evaluated by monitoring the resulting values of  $C_L$  and  $C_D$ . Once the variations in aerodynamic coefficients fall below the 2% threshold, the domain is considered sufficiently large and is fixed for the remainder of the study.

The results show that enlarging the domain beyond the selected configuration does not significantly affect the aerodynamic coefficients, confirming that boundary effects are negligible. The chosen domain size is therefore retained for all subsequent mesh convergence analyses and ground-effect simulations.

## 7.5 Mesh size convergence study

Mesh convergence is then investigated within the fixed computational domain. For each mesh level, steady-state simulations are performed until convergence, and the resulting lift and drag coefficients are extracted.

The evolution of  $C_L$  and  $C_D$  is analyzed as a function of the total number of cells. As the mesh is refined, both coefficients progressively approach asymptotic values, indicating convergence of the numerical solution.

The following images illustrate three representative mesh levels used in the convergence study for the case  $h/c = 1$ , highlighting the progressive refinement near the airfoil surface, in the wake region, and in the gap between the airfoil and the ground. .

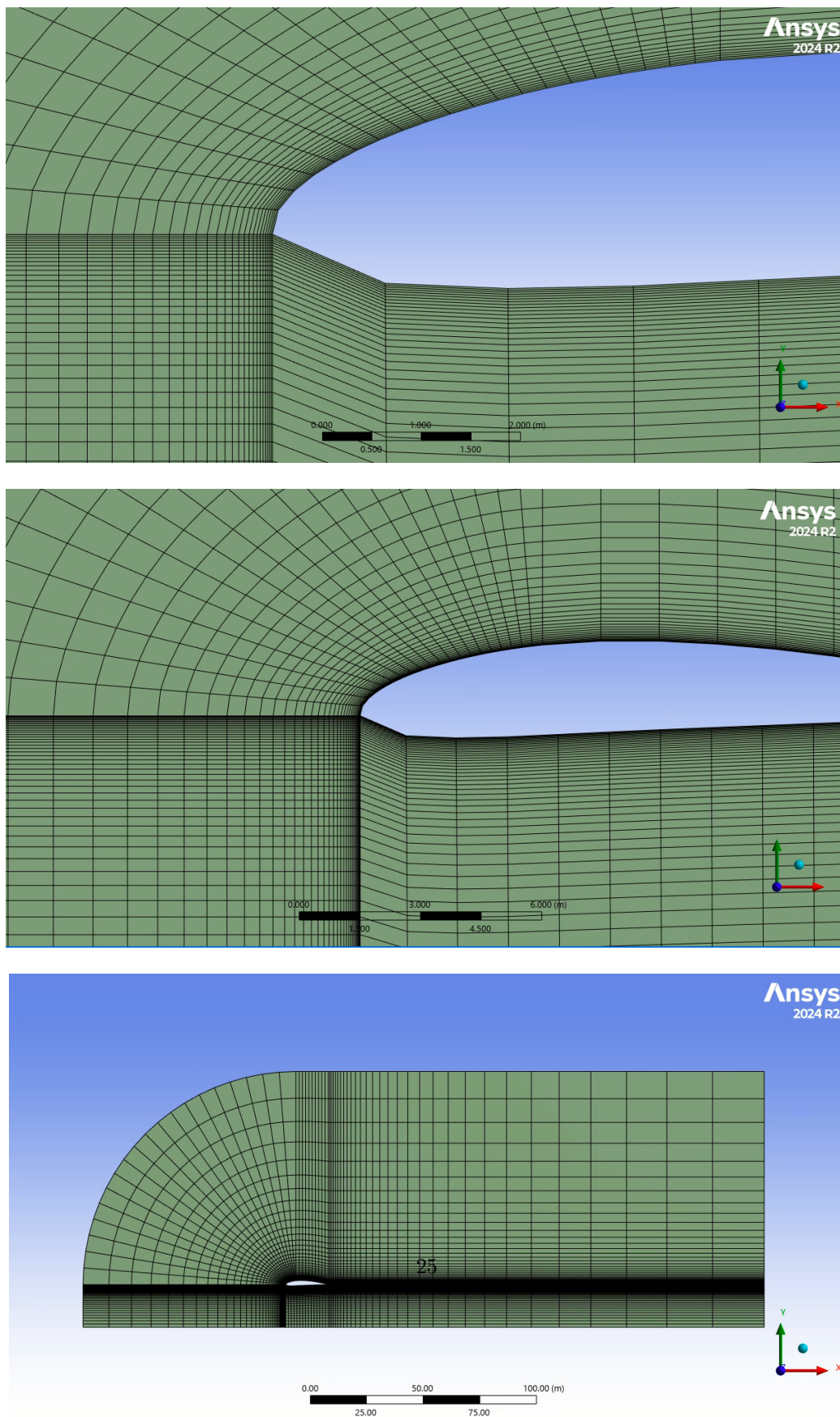


FIGURE 10 – Coarse mesh for  $h/c = 1$

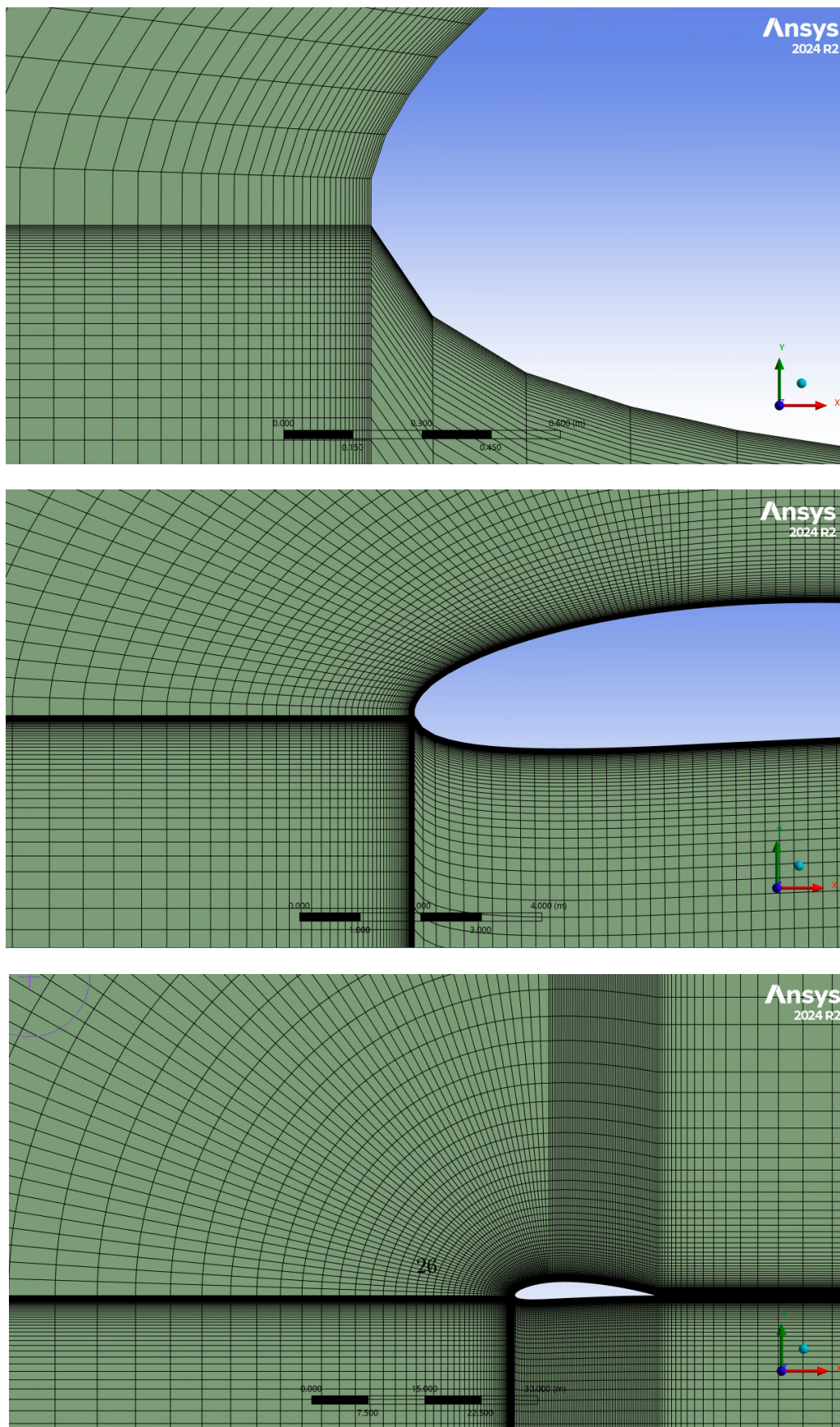


FIGURE 11 – Medium mesh for  $h/c = 1$

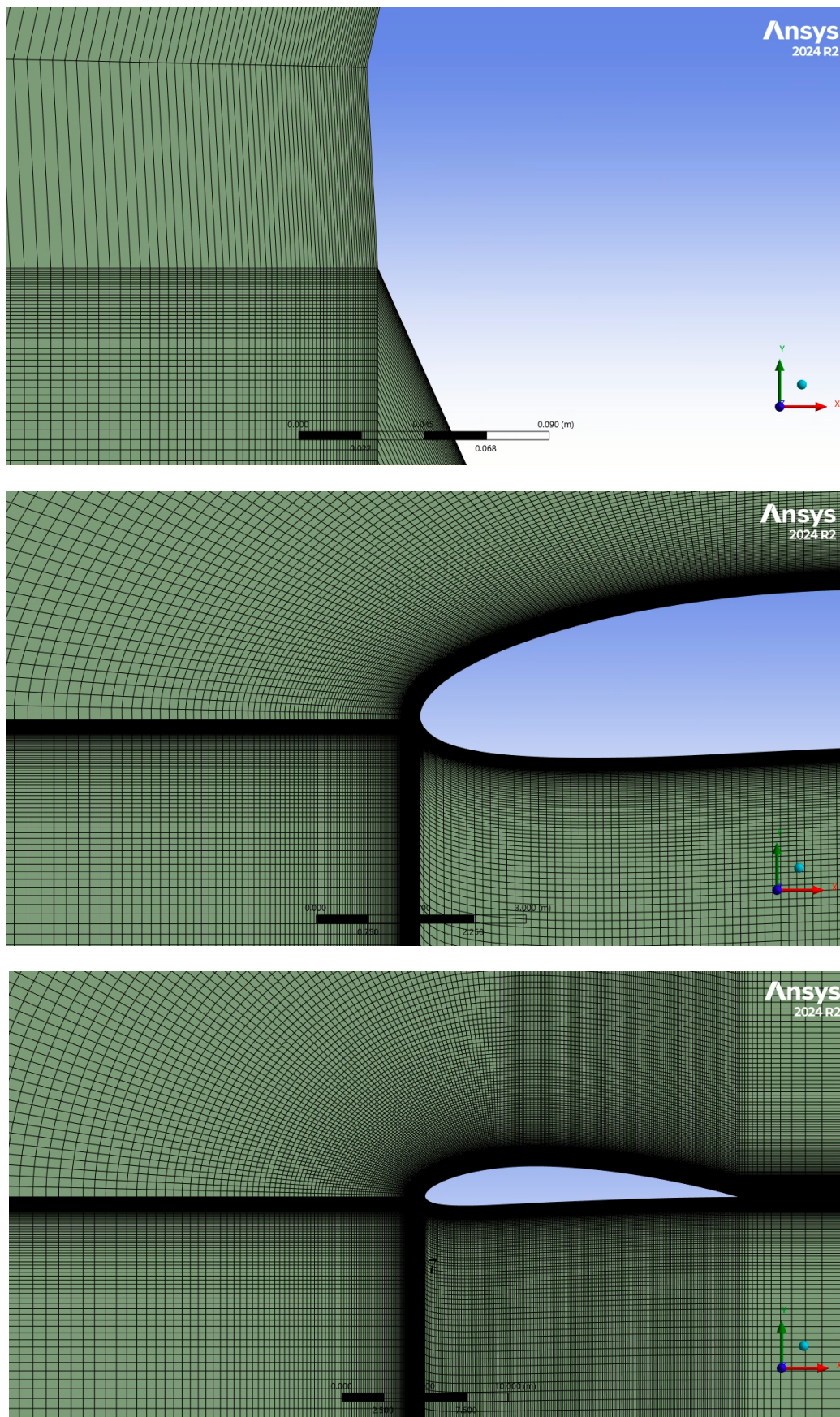


FIGURE 12 – Very fine mesh for  $h/c = 1$

The images below instead show two representative mesh resolutions considered in the convergence study for the configuration without ground effect, highlighting the progressive refinement around the airfoil surface and in the wake region.

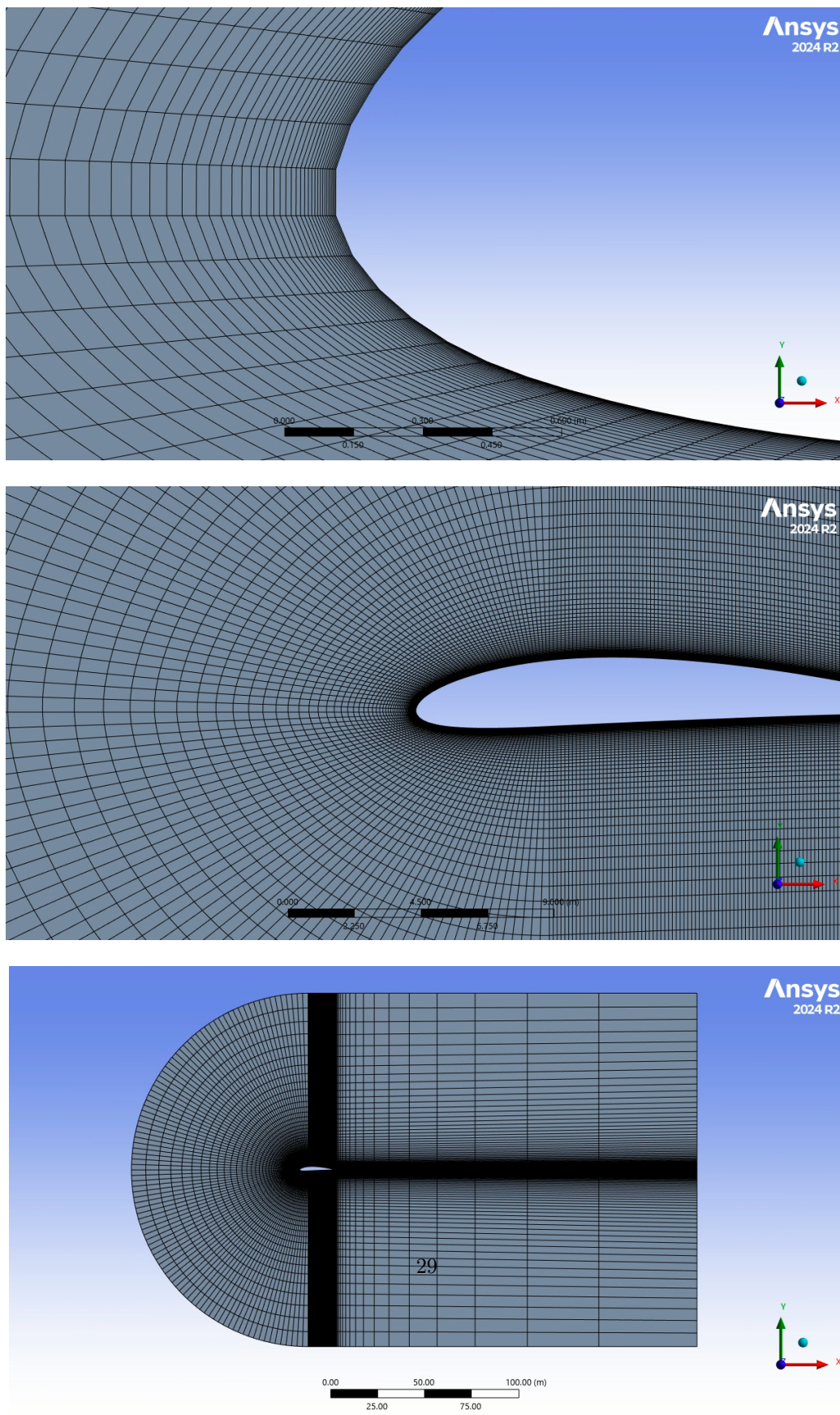


FIGURE 13 – Coarse mesh for the case without ground (infinite clearance)

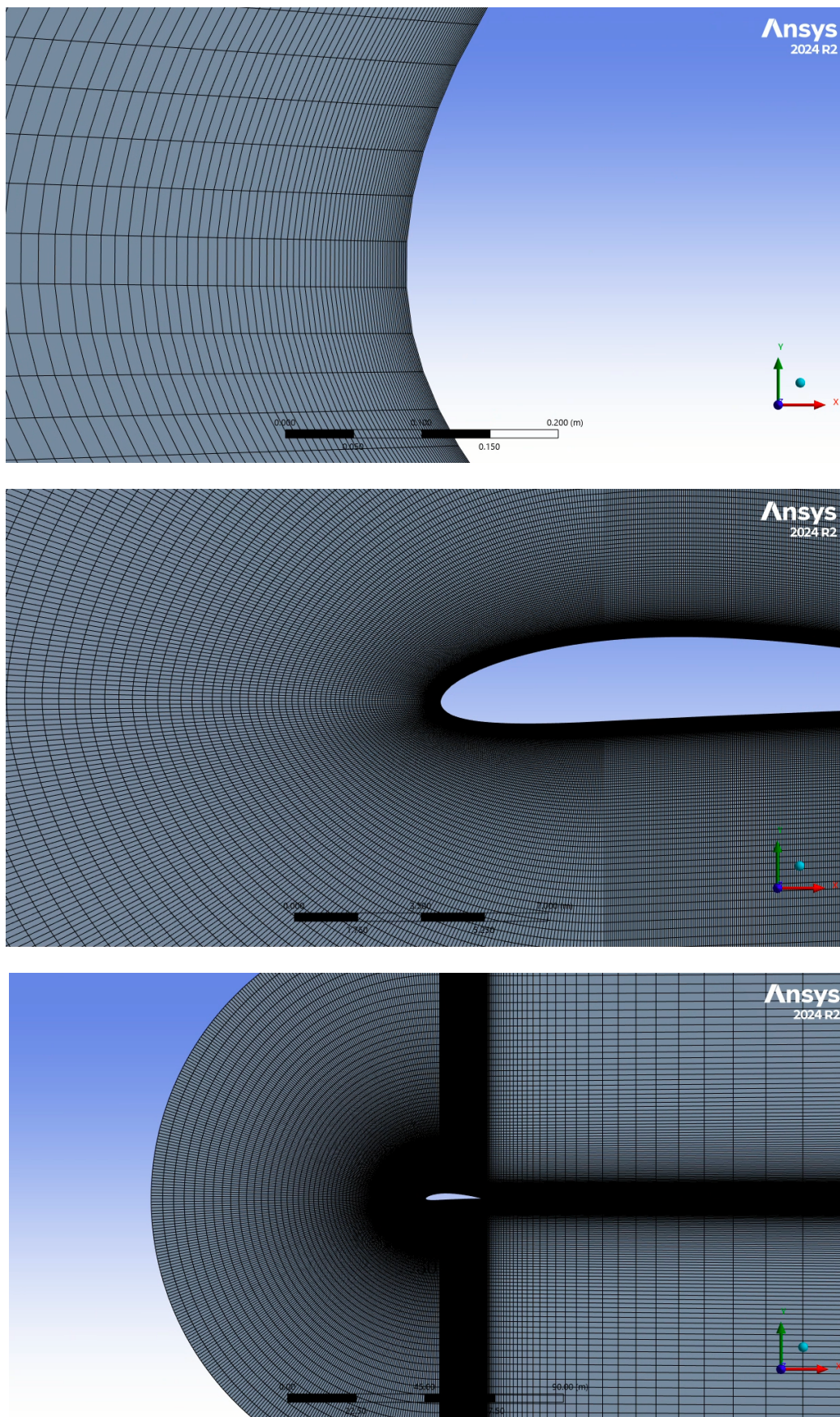


FIGURE 14 – Very fine mesh for the case without ground (infinite clearance)

## 7.6 Error estimation

To quantify discretization errors, both absolute and relative errors are evaluated for each mesh level. The absolute error is defined as the difference between the aerodynamic coefficient obtained on a given mesh and that obtained on the reference (previous) mesh. The relative error is defined as :

$$\varepsilon = \frac{|C - C_{\text{ref}}|}{C_{\text{ref}}}, \quad (10)$$

where  $C_{\text{ref}}$  denotes the value obtained on the finest mesh.

Table 4 summarizes the mesh sizes, aerodynamic coefficients, and associated absolute and relative errors for the mesh convergence study of the case  $h/c = 1$ .

Mesh level	Number of cells	$C_D$	$C_L$	Relative error $C_D$	Relative error $C_L$
Coarse	8345	0.0102	0.5235	—	—
Medium-Coarse	14650	0.0078	0.5154	23.5%	1.5%
Medium	24000	0.0061	0.4947	21.8%	4%
Medium-Fine	42800	0.0055	0.4950	9.8%	0.1%
Fine	72650	0.0054	0.4847	1.8%	2.1%
Very fine (ref.)	123250	0.0054	0.4928	0%	1.7%

TABLE 4 – Mesh convergence study for the  $h/c = 1$  configuration : lift and drag coefficients, absolute and relative errors with respect to the previous mesh.

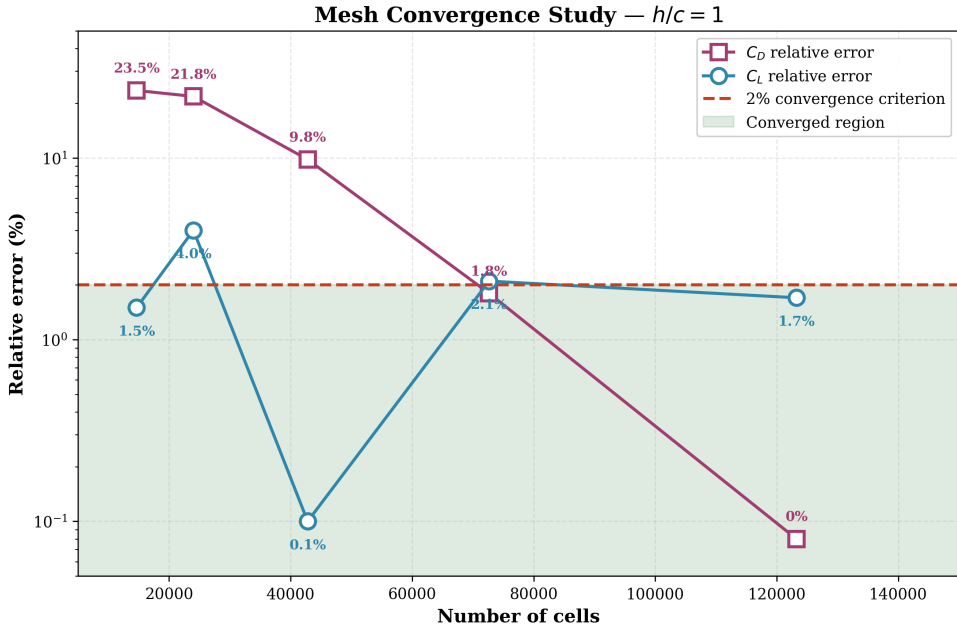


FIGURE 15 – Mesh convergence study for the  $h/c = 1$  configuration : relative errors for  $C_L$  and  $C_D$  with respect to the previous mesh level. The dashed line indicates the 2% convergence criterion.

For the configuration without ground effect, Table 5 presents the convergence of the numerical solution.

Mesh level	Number of cells	$C_D$	$C_L$	Relative error $C_D$	Relative error $C_L$
Coarse	33610	0.0068	0.4832	—	—
Medium	44540	0.0066	0.4802	2.9%	0.7%
Medium-Fine	64020	0.0064	0.4960	3%	3.3%
Fine	89992	0.0065	0.4794	1.6%	3.4%
Very fine (ref.)	126398	0.0065	0.4790	0%	0.1%

TABLE 5 – Mesh convergence study for the  $h/c = \infty$  configuration : lift and drag coefficients, absolute and relative errors with respect to the previous mesh.

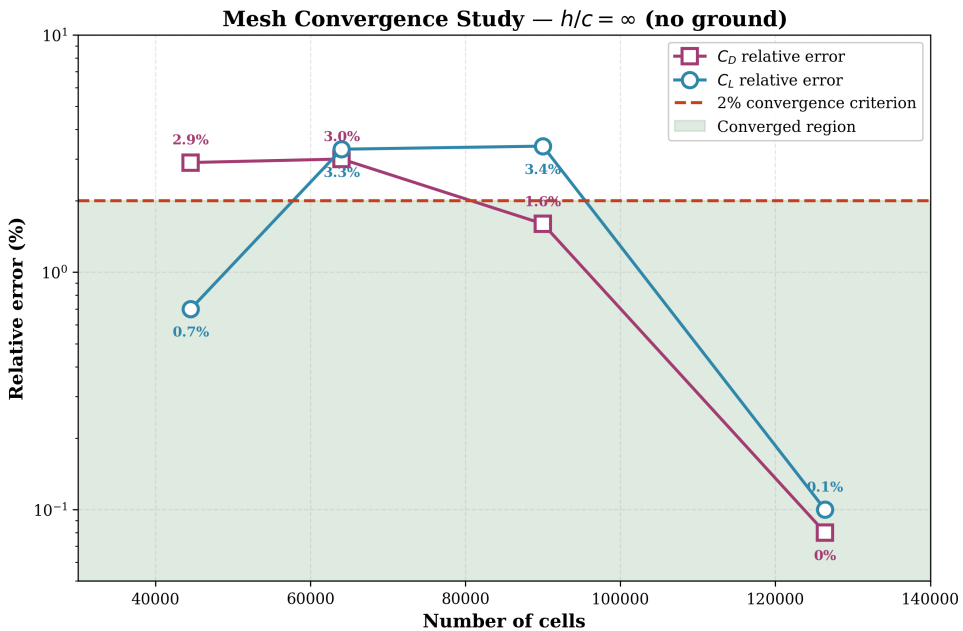


FIGURE 16 – Mesh convergence study for the  $h/c = \infty$  configuration : relative errors for  $C_L$  and  $C_D$  with respect to the previous mesh level.

Figure 17 provides an overview of the coefficient convergence behavior for both configurations, showing how  $C_L$  and  $C_D$  approach their asymptotic values as the mesh is refined.

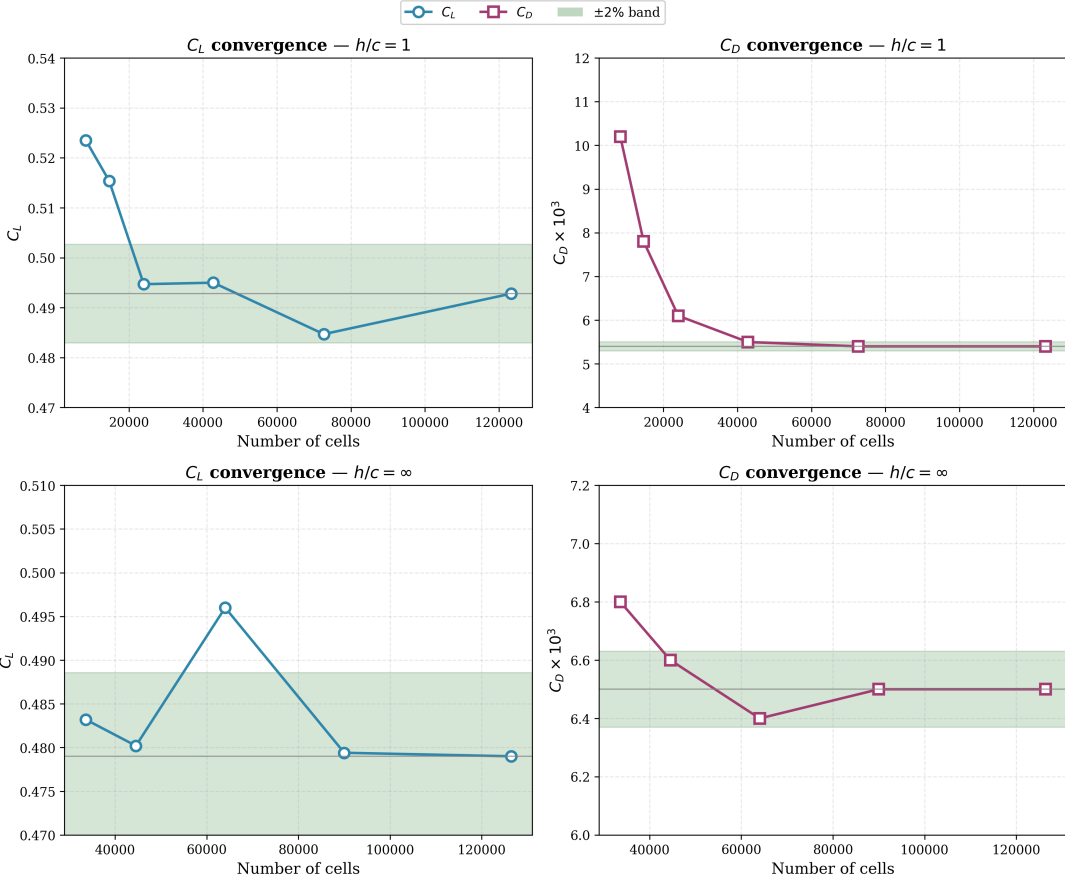


FIGURE 17 – Convergence of aerodynamic coefficients with mesh refinement :  $C_L$  (left) and  $C_D$  (right) for the  $h/c = 1$  configuration (top) and  $h/c = \infty$  configuration (bottom). The shaded bands represent the  $\pm 2\%$  convergence criterion.

## 7.7 Choice of the mesh and the domain

Based on the mesh convergence results, the coarsest mesh for which the relative errors on both  $C_L$  and  $C_D$  remain below the 2% threshold is selected as the final mesh for the study.

This mesh provides a compromise between numerical accuracy and computational cost. Together with the previously validated domain size, it is used for all ground-effect simulations presented in the following sections, ensuring that the observed variations in aerodynamic coefficients are driven by physical effects rather than numerical artifacts.

## 8 Results

### 8.1 Pressure and Velocity Contours

The pressure and velocity fields obtained from the simulations are presented below for different ground-clearance configurations. These contour plots illustrate the modification of the flow structure induced by the presence of the ground.

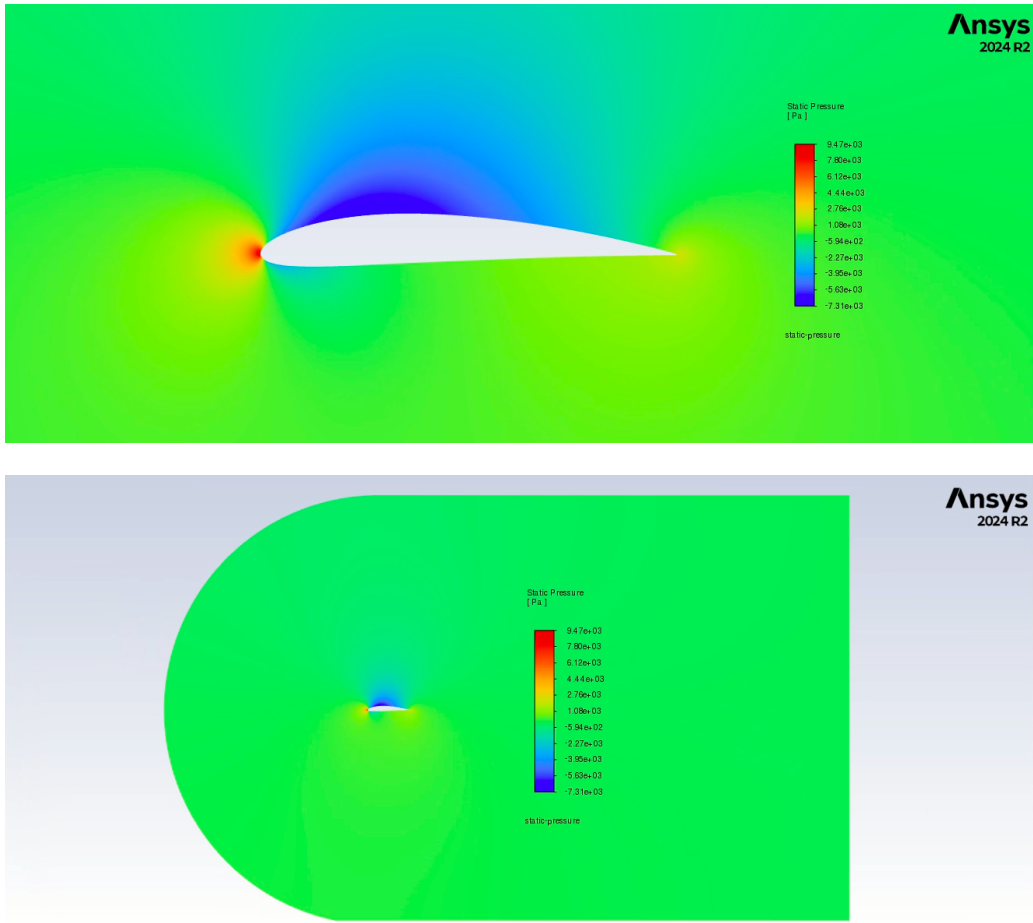


FIGURE 18 – Static pressure for the case no ground (infinite clearance)

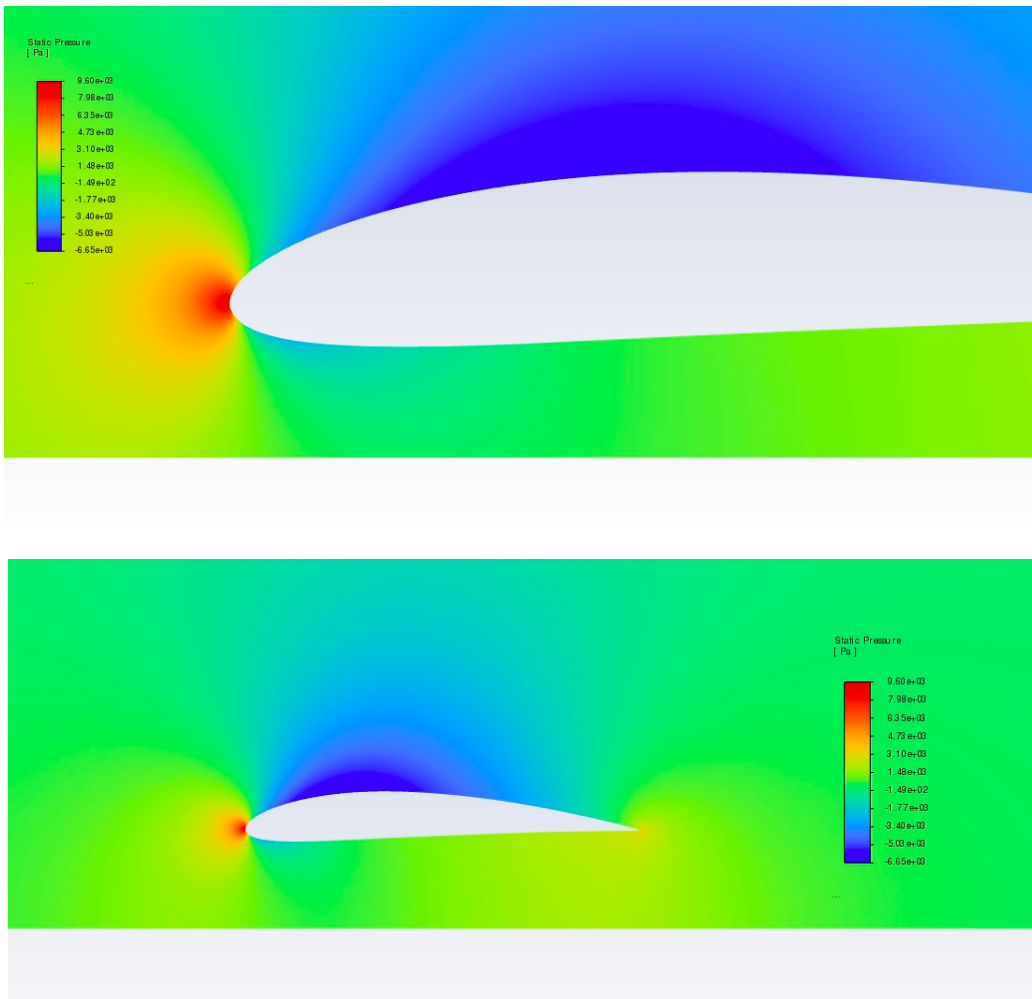
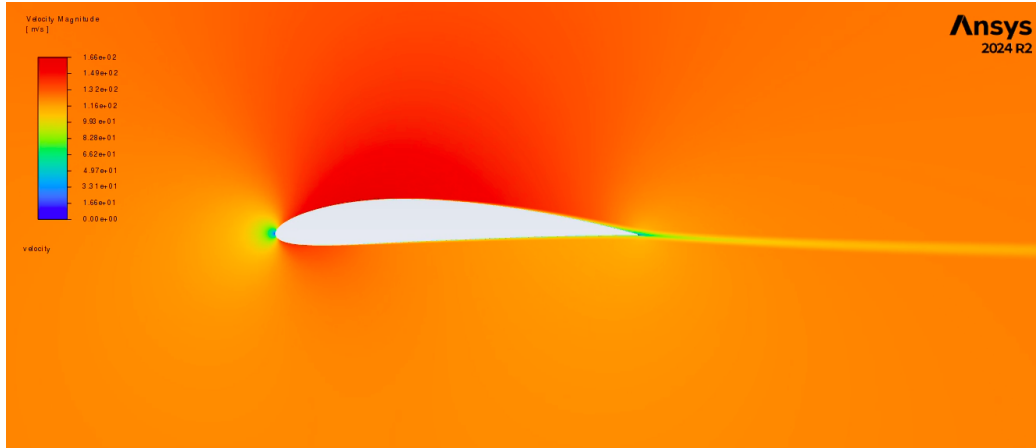
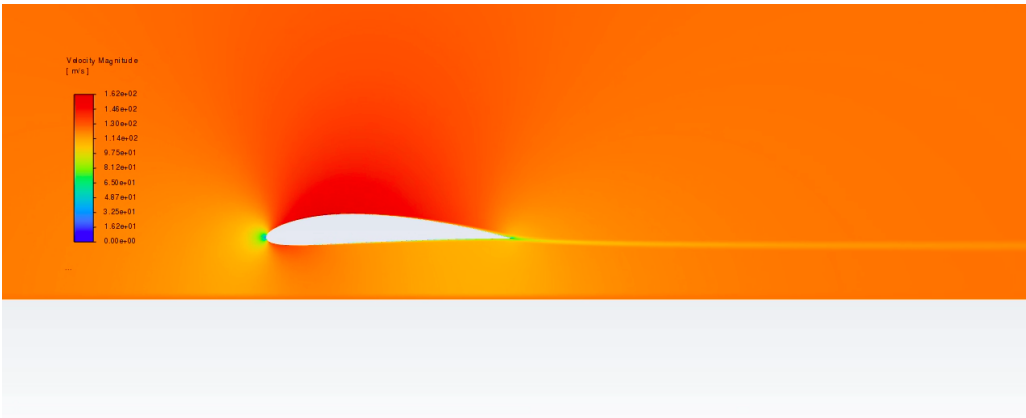


FIGURE 19 – Static pressure for the case  $h/c = 0.25$

As shown in the pressure contours above, the pressure field beneath the airfoil increases as the wing approaches the ground. Conversely, the pressure on the upper surface is reduced, resulting in an overall increase in lift.



(a) Magnitude velocity for the case no ground (infinite clearance)



(b) Magnitude velocity for the case  $h/c = 0.25$

FIGURE 20 – Velocity magnitude contours around the NACA 4412 airfoil for two extreme cases :  
(a) infinite clearance, and (b) minimum ground clearance  $h/c = 0.25$ .

Regarding the velocity field, a small reduction in flow speed is observed in the presence of the ground, as expected from ground effect considerations.

## 8.2 Aerodynamic Coefficients in Ground Effect

The aerodynamic coefficients obtained from the simulations are summarized in Table 6.

$h/c$	$C_D$	$C_L$	$C_L/C_D$
$\infty$ (no ground)	0.0065	0.479	73.7
2.0	0.0056	0.491	87.7
1.0	0.0054	0.493	91.3
0.5	0.0093	0.505	54.3
0.25	0.0101	0.510	50.5

TABLE 6 – Aerodynamic coefficients for different ground-clearance configurations.

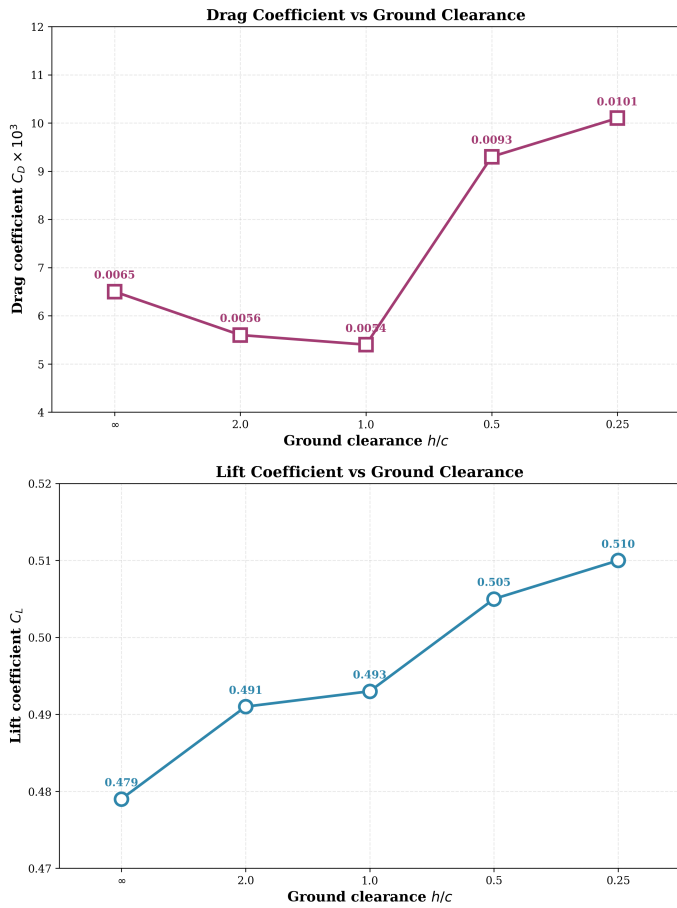


FIGURE 21 – Lift and Drag coefficient for different ground clearance values

As the airfoil approaches the ground, the drag coefficient initially decreases due to a reduction in

wake losses. At very low ground clearance, however, the flow becomes increasingly confined between the airfoil and the ground, leading to higher viscous shear and a consequent increase in drag. At the same time, the lift coefficient increases as a result of the higher pressure levels developing beneath the airfoil due to flow confinement, which is a characteristic feature of ground effect.

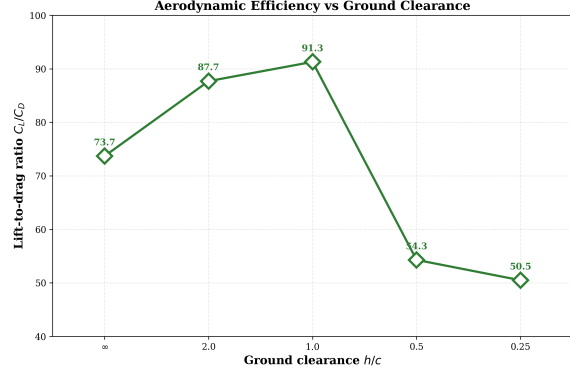


FIGURE 22 – Lift-to-Drag ratio for different ground clearance values

The evolution of the lift-to-drag ratio with ground clearance exhibits a non-monotonic behavior. Starting from the freestream configuration, the ratio  $C_L/C_D$  increases as the airfoil approaches the ground, reaching a maximum value at  $h/c = 1.0$ . This increase reflects the combined effect of lift enhancement and drag reduction at moderate ground clearance. For smaller values of  $h/c$ , the lift-to-drag ratio decreases, despite the continued increase in lift, due to the rapid growth of drag at very low ground clearance.

## 9 Analysis and Conclusions

### 9.1 Summary of Results

The present analysis demonstrates that the airfoil configuration representative of the Alexeyev KM ekranoplan benefits significantly from operating in ground effect. Compared to the freestream condition ( $h/c = \infty$ ), the aerodynamic coefficients are strongly influenced by the presence of the ground. Table 7 summarizes the main findings.

$h/c$	$C_L$	$\Delta C_L (\%)$	$C_D$	$C_L/C_D$
$\infty$	0.479	—	0.0065	73.7
2.0	0.491	+2.5	0.0056	87.7
1.0	0.493	+2.9	0.0054	91.3
0.5	0.505	+5.4	0.0093	54.3
0.25	0.510	+6.5	0.0101	50.5

TABLE 7 – Summary of aerodynamic coefficients and their variation with ground clearance.

The lift coefficient increases monotonically as the airfoil approaches the ground, in accordance with classical ground-effect theory. Starting from  $C_L = 0.479$  in the freestream case, the lift reaches  $C_L = 0.510$  at  $h/c = 0.25$ , corresponding to an enhancement of approximately 6.5%. This augmentation is attributed to the increased pressure beneath the airfoil caused by flow confinement, which modifies the pressure distribution and enhances the pressure difference across the airfoil.

The drag coefficient exhibits a non-monotonic behavior. From the freestream condition ( $C_D = 0.0065$ ), the drag initially decreases to a minimum of  $C_D = 0.0054$  at  $h/c = 1.0$  (a 17% reduction), then increases sharply at lower clearances, reaching  $C_D = 0.0101$  at  $h/c = 0.25$  (a 55% increase relative to freestream).

### 9.2 Drag Behavior at Low Ground Clearance

The increase in drag observed at very low ground clearance ( $h/c < 1.0$ ) is the result of several coupled aerodynamic mechanisms and cannot be attributed solely to viscous effects.

As the airfoil approaches the ground, the flow in the gap between the lower surface and the ground becomes increasingly confined. In order to satisfy mass conservation, the local flow velocity in this region increases, leading to steep velocity gradients normal to both the airfoil surface and the ground. This results in a significant increase in viscous shear stress, which directly contributes to higher skin-friction drag.

In addition to viscous effects, pressure drag also plays an important role at very low ground clearance. The confinement of the flow leads to an increase in the mean static pressure beneath the airfoil, particularly upstream of the trailing edge. While this pressure rise contributes positively to lift, it can also alter the pressure distribution near the trailing edge in an unfavorable manner, reducing pressure recovery and increasing pressure drag.

Furthermore, the presence of the ground modifies the wake structure downstream of the airfoil. At very low  $h/c$ , the wake tends to become thicker and more asymmetric due to the constrained outflow from the gap region. This altered wake structure is associated with additional momentum losses and contributes to the observed increase in total drag.

At the high Reynolds number considered in this study ( $\text{Re} \approx 1.6 \times 10^8$ ), viscous effects remain confined to thin boundary layers ; however, the large dynamic pressure amplifies the contribution of both viscous shear and pressure forces to the overall drag. As a result, the drag penalty associated with extreme ground proximity can outweigh the aerodynamic benefits of lift enhancement.

It should also be noted that the numerical prediction of drag at very low ground clearance is particularly sensitive to mesh resolution and near-wall treatment in the confined gap region. Although mesh convergence has been verified, the  $h/c = 0.25$  case represents the most challenging configuration from a numerical standpoint, and the corresponding drag values should therefore be interpreted with appropriate caution.

### 9.3 Comparison with Experimental Literature

Ahmed et al. [7] conducted an experimental investigation of the NACA 4412 airfoil in ground effect at Reynolds numbers between  $2.4 \times 10^5$  and  $3.0 \times 10^5$ , corresponding to freestream velocities of approximately 20–25 m/s. Although direct quantitative comparison is limited by the significant difference in Reynolds number (three orders of magnitude lower than the present study), their results provide valuable qualitative insight.

- **Lift enhancement :** Ahmed et al. reported a monotonic increase in  $C_L$  with decreasing ground clearance at all tested angles of attack, consistent with the present findings. At  $\alpha = 0^\circ$ , they observed lift increases of approximately 10–15% at  $h/c = 0.1$ , somewhat higher than the 6.5% increase found here at  $h/c = 0.25$ . This difference may be attributed to the different Reynolds number regimes and the associated changes in boundary-layer behavior.
- **Drag behavior :** At low Reynolds numbers, Ahmed et al. observed a continuous decrease in drag coefficient as ground clearance decreased, attributed to improved pressure recovery beneath the airfoil. In contrast, the present high-Reynolds-number simulations show a drag increase at  $h/c < 1.0$ . This discrepancy can be explained by the different relative importance of viscous effects : at  $\text{Re} \sim 10^5$ , pressure drag dominates and benefits from ground proximity ; at  $\text{Re} \sim 10^8$ , viscous drag becomes more significant, and the intense shear in the confined gap leads to increased dissipation.
- **Optimal ground clearance :** Ahmed et al. did not identify a drag minimum at moderate clearances, as their low-Reynolds-number conditions favored continuous drag reduction with decreasing  $h/c$ . The present study identifies an optimal clearance at  $h/c \approx 1.0$ , where the balance between lift enhancement and viscous drag penalty yields maximum aerodynamic efficiency ( $C_L/C_D = 91.3$ ).

These comparisons underscore that ground-effect aerodynamics is strongly dependent on the Reynolds number regime. Results obtained at low Reynolds numbers cannot be directly extrapolated to high-speed, high-Reynolds-number applications such as the Alexeyev KM ekranoplan.

### 9.4 Accuracy and Limitations

From a numerical perspective, the simulation results are considered accurate and converged. Convergence was assessed through residual reduction, stabilization of aerodynamic coefficients, and verification of mass flow balance. The computed coefficients reached stable plateaus for all investigated ground clearances.

At the lowest ground clearance, a slight asymmetry of the wake is observed. Since the simulations are steady-state, this feature represents a steady asymmetric flow pattern associated with strong confinement rather than physical wake oscillations. Nevertheless, the integrated aerodynamic coefficients remain stable, supporting the validity of the steady-state approach.

The analysis is restricted to a two-dimensional formulation and therefore focuses on the aerodynamic behavior of an isolated airfoil section. As a consequence, inherently three-dimensional phenomena such as induced drag, wingtip vortices, and spanwise flow redistribution are not captured. While this limitation does not invalidate the observed trends in lift and drag variations with ground clearance, it affects the quantitative interpretation of the results, particularly at very low ground clearance where three-dimensional effects play a dominant role in real configurations.

## 9.5 Implications for Real Ground-Effect Vehicles

The optimal ground clearance identified in this study ( $h/c \approx 1.0$ , corresponding to  $h \approx 18.8$  m) should not be interpreted as an optimal operating altitude for the real Alexeyev KM ekranoplan. Several factors must be considered :

1. **Induced drag** : In a real three-dimensional vehicle, induced drag constitutes a dominant component of total drag. This contribution is strongly reduced in ground effect due to suppression of downwash and wingtip vortices. As a result, the overall drag behavior of a 3D vehicle may differ significantly from the viscous-dominated trends observed at the sectional level.
2. **Operational constraints** : The actual flight height of the KM was governed not only by aerodynamic efficiency but also by structural constraints, stability and control requirements, wave clearance over rough seas, and safety considerations.
3. **Three-dimensional benefits** : The beneficial reduction of induced drag at low altitude in 3D flow may compensate for the viscous drag increase observed in the present 2D simulations, potentially shifting the optimal operating point to lower clearances than predicted here.

## 9.6 Conclusions

The present study provides a physically consistent interpretation of ground-effect aerodynamics at the airfoil-section level. The numerical results demonstrate that ground proximity strongly modifies the aerodynamic performance of the airfoil, leading to a monotonic lift increase and a non-monotonic drag response as the ground clearance is reduced. While flying very close to the ground maximizes lift locally, the simulations indicate that operating at moderate ground clearance offers the best compromise between lift enhancement and drag reduction within the simplified two-dimensional framework.

The identified optimal clearance ( $h/c \approx 1.0$ ) should be interpreted strictly as a sectional result. In real ground-effect vehicles such as the Alexeyev KM ekranoplan, additional mechanisms—most notably three-dimensional effects and the associated reduction of induced drag—play a dominant role and may significantly alter the balance between lift and drag at low altitude. Furthermore, operational constraints related to stability, structural loads, wave clearance, and safety ultimately govern the achievable flight height of such vehicles. Available documentation and flight-test footage indicate that the KM typically operated at altitudes of the order of approximately 4 to 18 m above the water surface, corresponding to a regime of moderate ground effect rather than extreme near-surface flight. Another consideration to take into account is the fact that the actual wing profile

may not be a NACA 4412, since these data are secret and therefore approximate. A different wing profile with an angle of attack other than zero could result in different values of  $C_L$  and  $C_D$ .

When interpreted in conjunction with these three-dimensional effects and real-world operational considerations, the present findings remain consistent with the general aerodynamic principles underlying the design and operation of the Alexeyev KM ekranoplan. The study thus offers a sound qualitative basis for understanding ground-effect aerodynamics, while clearly delineating the limits of applicability of a two-dimensional numerical approach.

## 9.7 Recommendations

Based on the present study, several improvements can be recommended for future investigations of ground-effect aerodynamics. From a numerical perspective, extending the analysis to a compressible flow formulation would allow the influence of density variations to be quantified and would reduce modeling uncertainty at moderate Mach numbers.

From a physical modeling standpoint, three-dimensional simulations of a finite wing would enable the combined effects of ground proximity and induced drag reduction to be assessed, providing a more realistic representation of real ground-effect vehicles. Finally, a systematic decomposition of viscous and pressure drag contributions would offer deeper insight into the mechanisms governing drag behavior in extreme ground-effect conditions.

## 10 Appendix

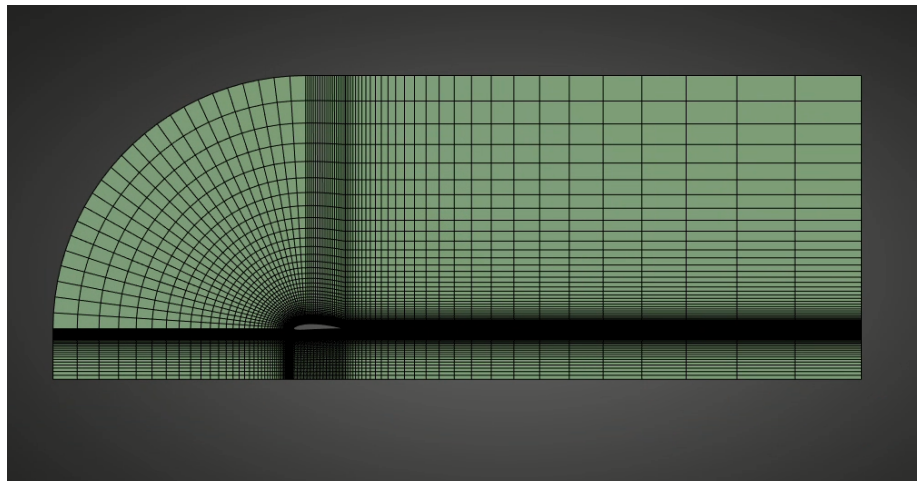


FIGURE 23 – Medium-Coarse mesh for  $h/c = 1$

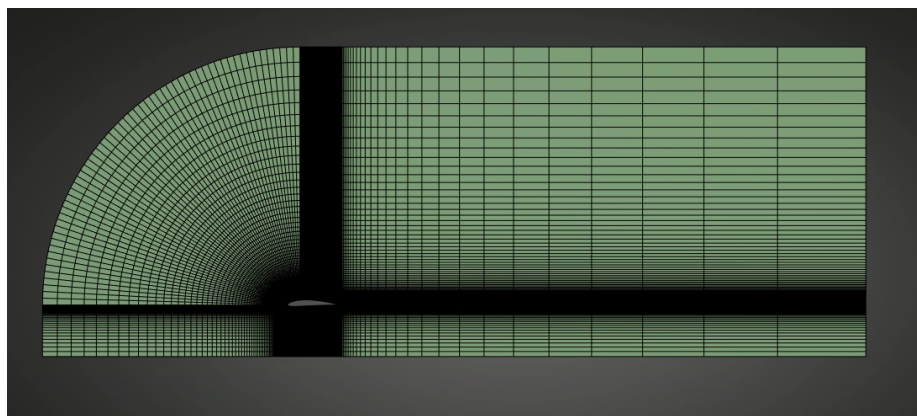


FIGURE 24 – Medium-Fine mesh for  $h/c = 1$

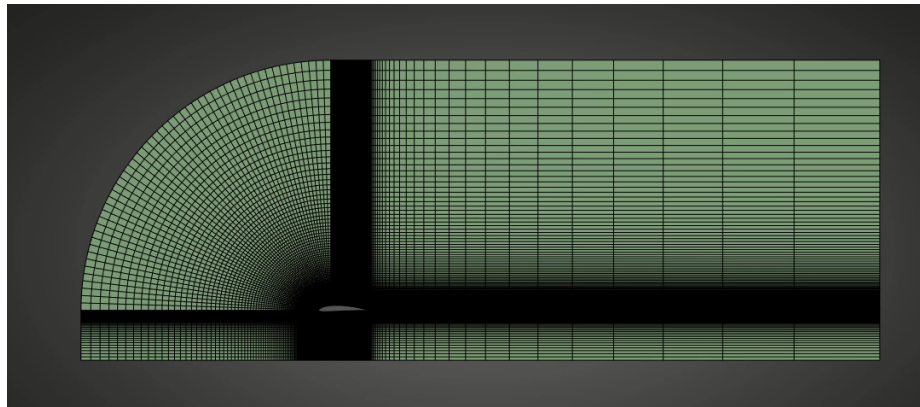


FIGURE 25 – Fine mesh for  $h/c = 1$

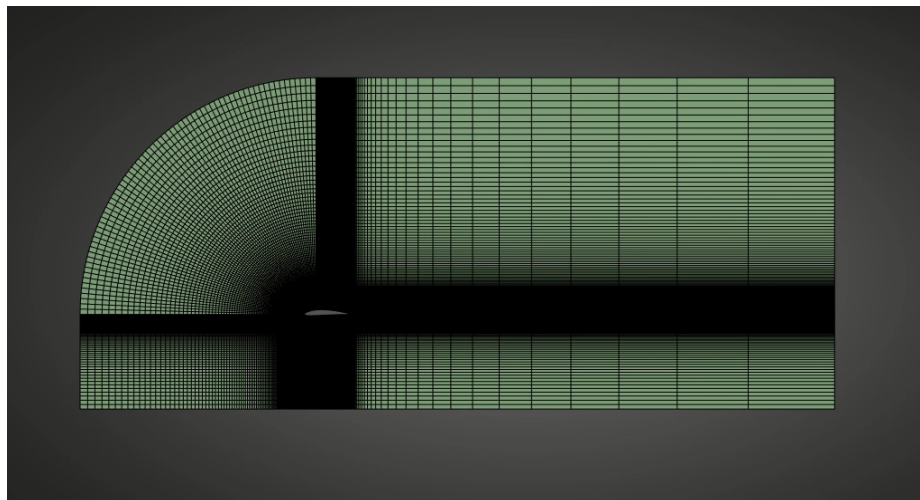


FIGURE 26 – Mesh for  $h/c = 2$

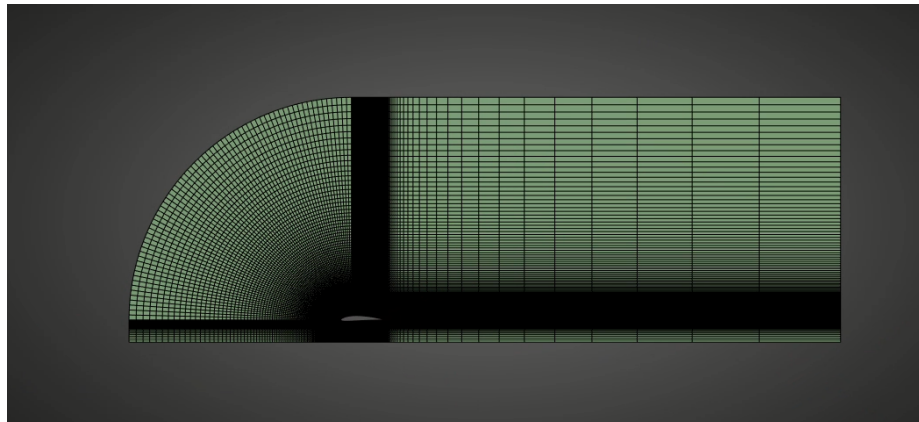


FIGURE 27 – Mesh for  $h/c = 0.5$

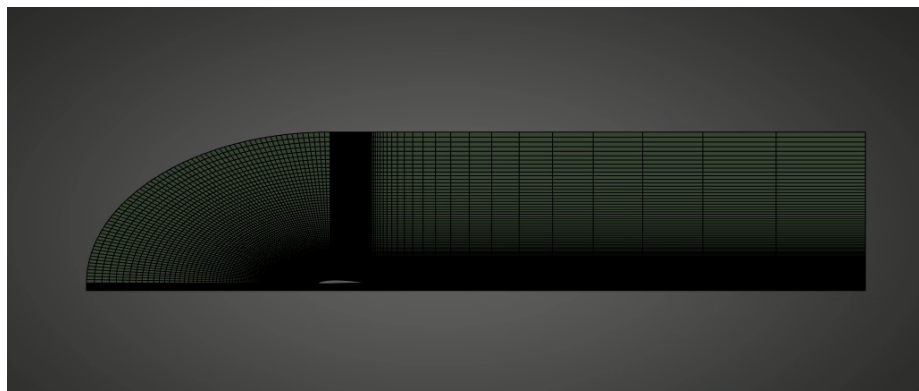


FIGURE 28 – Mesh for  $h/c = 0.25$

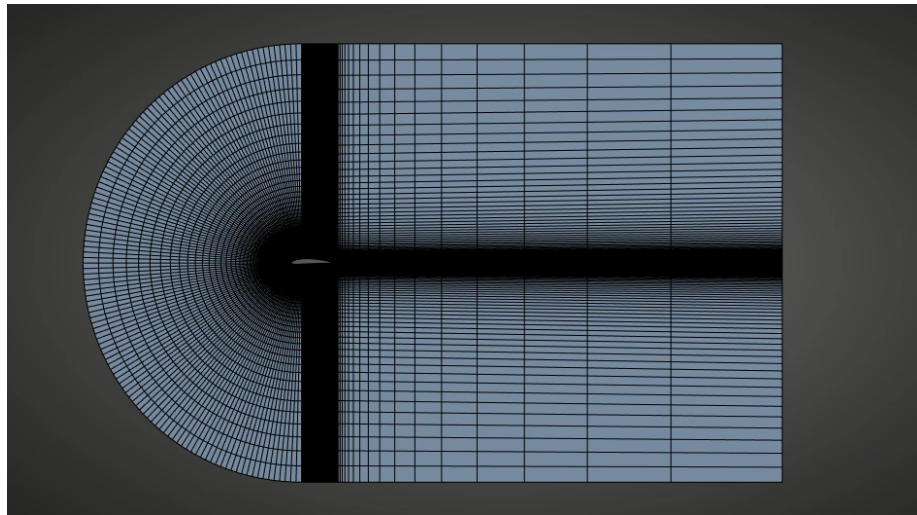


FIGURE 29 – Medium mesh for  $h/c = \infty$

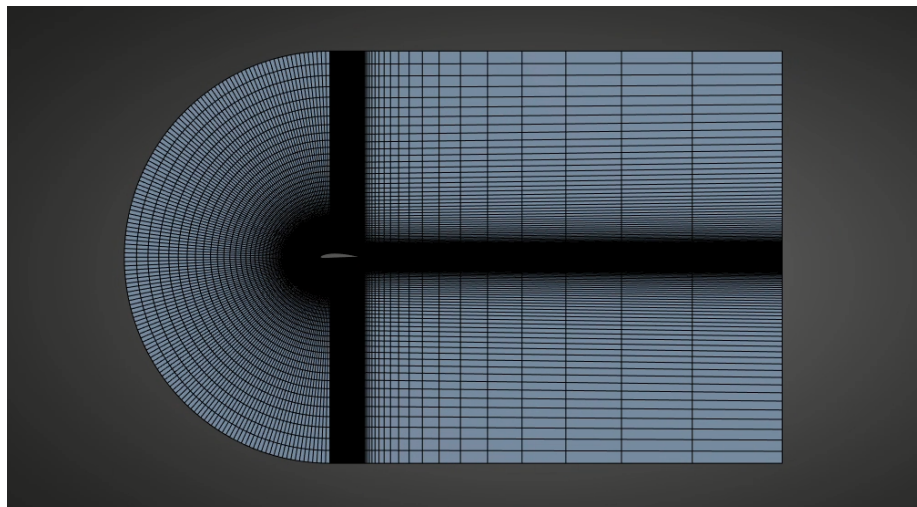


FIGURE 30 – Medium-Fine mesh for  $h/c = \infty$

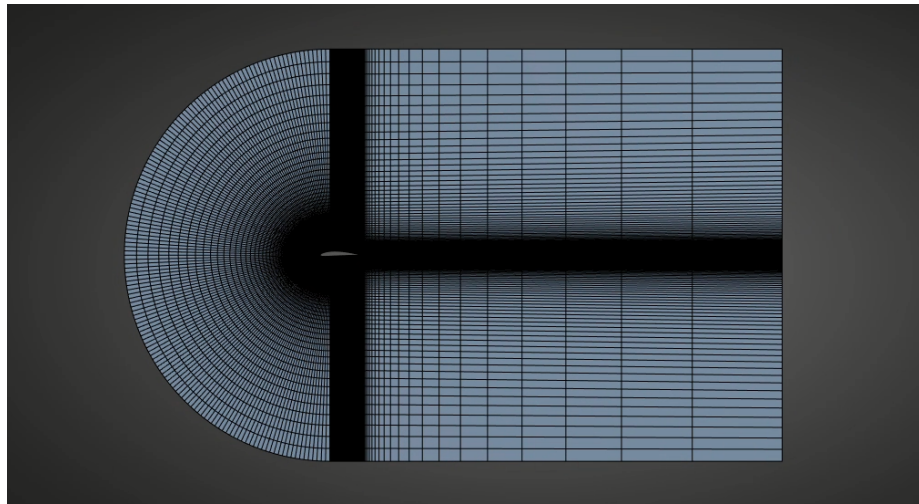


FIGURE 31 – Fine mesh for  $h/c = \infty$

## Références

- [1] ME-474 Numerical Flow Simulation Course Notes
- [2] Wikipedia contributors, *Caspian Sea Monster (KM Ekranoplan)*, Wikipedia, The Free Encyclopedia, [https://en.wikipedia.org/wiki/Caspian\\_Sea\\_Monster](https://en.wikipedia.org/wiki/Caspian_Sea_Monster), accessed on 15 Nov 2025.
- [3] E. C. Maskell, *A theory of the effect of ground proximity on the aerodynamic characteristics of wings*, Aeronautical Research Council Reports and Memoranda No. 3681, 1972.
- [4] C. H. Liu and V. C. Patel, *Aerodynamics of wings in ground effect*, AIAA Journal, Vol. 20, No. 9, pp. 1266–1272, 1982.
- [5] C. M. Hsien and C. K. Chen, *Aerodynamic characteristics of airfoils in ground effect*, Journal of Aircraft, Vol. 33, No. 2, pp. 386–392, 1996.
- [6] M. R. Ahmed and S. D. Sharma, *An investigation on the aerodynamics of a symmetric airfoil in ground effect*, Experimental Thermal and Fluid Science, Vol. 29, pp. 633–647, 2005.
- [7] M. R. Ahmed, T. Takasaki, and Y. Kohama, *Aerodynamics of a NACA4412 Airfoil in Ground Effect*, AIAA Journal, Vol. 45, No. 1, pp. 37–47, 2007.
- [8] Q. Qu, Z. Wang, and Y. Wu, *Numerical investigation of ground effect on airfoil aerodynamic performance*, Aerospace Science and Technology, Vol. 43, pp. 75–86, 2015.
- [9] K. V. Rozhdestvensky, *Wing-in-ground effect vehicles*, Progress in Aerospace Sciences, Vol. 42, pp. 211–283, 2006.
- [10] A. E. Ockfen and K. I. Matveev, *Aerodynamic characteristics of NACA airfoils in ground effect*, Journal of Aircraft, Vol. 46, No. 4, pp. 1254–1262, 2009.
- [11] AirfoilTools, *NACA 4412 Airfoil Coordinates and Data*, <http://airfoiltools.com/airfoil/details?airfoil=naca4412-il>, accessed on 20 Nov 2025.

- [12] NASA Glenn Research Center, *Isentropic Flow Equations*,  
<https://www.grc.nasa.gov/www/k-12/airplane/isentrop.html>, accessed on 29 Dec 2025.
- [13] J. D. Anderson, *Fundamentals of Aerodynamics*, 5th ed., McGraw-Hill, New York, 2011.
- [14] H. K. Versteeg and W. Malalasekera, *An Introduction to Computational Fluid Dynamics : The Finite Volume Method*, 2nd ed., Pearson Education, 2007.
- [15] ANSYS Inc., *ANSYS Fluent Theory Guide*, Release 2024 R1.
- [16] P. R. Spalart and S. R. Allmaras, *A one-equation turbulence model for aerodynamic flows*, AIAA Paper 92-0439, 1992.
- [17] OpenAI, ChatGPT : language model for content assistance and text refinement,  
<https://chat.openai.com>, accessed on 28 Dec 2025.
- [18] Anthropic, Claude : AI assistant for content assistance and text refinement,  
<https://claude.ai>, accessed on 29 Dec 2025.